ÉCOLE POLYTECHNIQUE
FÉDÉRALE DE LAUSANNE

MATHICSE
Mathematics Institute of Computational Science and Engineering
School of Basic Sciences - Section of Mathematics

MATHICSE Technical Report
Nr. 10.2012
February 2012

Implicit coupling of one-dimensional and three-dimensional blood flow models with compliant vessels

Cristiano Malossi, Pablo Blanco, Paolo Crosetto, Simone Deparis, Alfio Quarteroni

http://mathicse.epfl.ch

Phone: +41 21 69 37648

Address:
EPFL - SB - MATHICSE (Bâtiment MA)
Station 8 - CH-1015 - Lausanne - Switzerland

Fax: +41 21 69 32545

IMPLICIT COUPLING OF ONE-DIMENSIONAL AND THREE-DIMENSIONAL BLOOD FLOW MODELS WITH COMPLIANT VESSELS

A. CRISTIANO I. MALOSSI[†], PABLO J. BLANCO[‡§], PAOLO CROSETTO[†], SIMONE DEPARIS[†], AND ALFIO QUARTERONI[†¶]

Abstract. Simulating arterial trees in the cardiovascular system can be made by the help of different models, depending on the outputs of interest and the desired degree of accuracy. In particular, one-dimensional fluid-structure interaction models for arteries are very effective in reproducing the physiological pressure wave propagation and in providing quantities like pressure and velocity, averaged on the cross section of the arterial lumen. In locations where one-dimensional models cannot capture the complete flow dynamics, e.g., in presence of stenoses and aneurysms, three-dimensional coupled fluid-structure interaction models are necessary to evaluate, for instance, critical factors responsible for pathologies which are associated to hemodynamics. In this work we formalize and investigate the geometrical multiscale problem, where heterogeneous fluid-structure interaction models for arteries are implicitly coupled. We introduce new coupling algorithms, describe their implementation and investigate on simple geometries the numerical reflections that occur at the interface between the heterogeneous models. We also simulate on a supercomputer a three-dimensional abdominal aorta under physiological conditions, coupled with up to six one-dimensional models representing the surrounding arterial branches. Finally, we compare CPU times and number of coupling iterations for different algorithms and time discretizations.

Key words. Blood flow models, geometrical multiscale modeling, coupling conditions, fluid-structure interaction, wave propagation.

AMS subject classifications. 65M60, 74F10, 76D05, 92C35.

1. Introduction.

Research in the field of hemodynamics is essential in order to understand, predict, and treat very common and dangerous cardiovascular pathologies, such as aneurysms formation, atherosclerosis, and congenital defects. Numerical simulations of blood flow dynamics constantly improve in terms of reliability, efficiency and model complexity. In this work we address the problem of simulating accurately and efficiently the blood flow in the large arteries of the systemic circulation.

Since some of the indicators for pathologies, e.g., the pulse wave velocity, are consequence of the vessel wall compliance, the deformation of the vessel has to be taken into account to have meaningful simulations and to draw reliable conclusions. Modeling the corresponding Fluid-Structure Interaction (FSI) can be achieved in several ways, e.g., using a one-dimensional (1-D) model for the whole vessel (see, for instance, [1, 2, 3]), performing a three-dimensional (3-D) simulation for the fluid inside the lumen, with a two-dimensional (2-D) structure represented by a proper boundary condition at the endothelial wall (see, for instance, [4, 5, 6]), or modeling the interaction between the 3-D blood flow and a 3-D vessel wall by coupling the equations for

[†]CMCS, Chair of Modelling and Scientific Computing, MATHICSE, Mathematics Institute of Computational Science and Engineering, EPFL, École Polytechnique Fédérale de Lausanne, Station 8, CH-1015, Lausanne, Switzerland (cristiano.malossi@epfl.ch, paolo.crosetto@epfl.ch, simone.deparis@epfl.ch, and alfio.quarteroni@epfl.ch).

[‡]LNCC, Laboratório Nacional de Computação Científica, Av. Getúlio Vargas 333, Quitandinha, 25651-075, Petrópolis, Brazil (pjblanco@lncc.br).

[§]INCT-MACC, Instituto Nacional de Ciência e Tecnologia em Medicina Assistida por Computação Científica, Petrópolis, Brazil.

[¶]MOX, Modeling and Scientific Computing, Department of Mathematics, Politecnico di Milano, Via Bonardi 9, Milan, Italy.

the fluid flow with those for a solid structure (see [7, 8, 9, 10, 11, 12] and references therein).

Being the time constraint important in a medical environment, a compromise between model complexity and computational cost is mandatory. For this reason only few specific components of the problem are represented by 3-D models, while the remaining parts are in general accounted for through reduced models. More precisely, 1-D models are used to represent network of arteries (see, for instance, [13, 14]), while the heart and its valves, the veins, and the peripheral circulation are in general accounted through lumped models (see [15, 16] and references therein). The coupling of these heterogeneous models is what we call the geometrical multiscale problem. Its efficient solution is a challenging task which has been addressed by several research groups with the final goal of accounting for the whole circulation and autoregulation (see, for instance, [6, 17, 18, 19]).

In this work we propose different methods to handle the coupling of the heterogeneous FSI models. More precisely, first we address the coupling of the fluid part of the problem, which can be set up by imposing different types of quantities at the coupling interfaces [20]. Then we focus on the solid part: here, the 3-D solid problem requires an additional set of boundary conditions on the interfaces rings, while the 1-D problem is already closed thanks to the local relation between the pressure and the area of the vessel. To close the 3-D solid problem we propose several approaches. Among them, we also devise a technique to impose the continuity of the area with the surrounding reduced models, extending the work done in [21]. These conditions are often neglected in literature, also due to their non trivial implementation.

One of the main concerns when dealing with geometrical multiscale problems is the need to avoid numerical spurious reflections at the interface separating the two models (see [22, 23]). Therefore, we study the influence of the proposed interface conditions on the amplitude of the spurious backward reflections that eventually arise at the coupling interfaces between two dimensionally-heterogeneous pipes. In order to have a full overview of the phenomena we analyze both the case of a 1-D wave flow that enters in a 3-D pipe, and the inverse one, i.e., a 3-D wave flow that enters in a 1-D pipe. The former case is considered here for the first time at the best of our knowledge. In fact our goal is not only to devise a set of boundary conditions that absorb the numerical reflections in a 3-D simulation, but more generally to embed 3-D pieces in a 1-D network in order to be able to perform 3-D simulations within a consistent hemodynamics environment, in terms of upstream and downstream vascular impedances, provided by a proper 1-D model.

In addition, we also study the computational efficiency of the solution of the global coupled problem. In a network composed of 1-D models we insert a real 3-D geometry of the abdominal aorta. This results in six coupling interfaces between 1-D FSI models and one 3-D FSI model. For this physiological test case we consider two different time discretizations for the 3-D FSI problem and two different methods to solve the coupling between the models. We compare the CPU time for all these options and we investigate its dependence on the number of 1-D pieces considered for the coupling.

The methodology described in this work for the coupling of the heterogeneous models has been implemented as part of the `C++` finite elements library `LifeV`[1], which is distributed under LGPL licence. Efficient and parallel solvers for 3-D FSI ([12, 24]) and 1-D FSI ([14]) problems have been exploited and coupled within a single general

[1] www.lifev.org

and extensible framework. In addition, the parallel implementation allows us to tackle large problems and to profitably use scalable supercomputers. The results of this work have been later used in [25] for the study of the physical consistency of the coupling between 3-D and 1-D FSI models for cardiovascular applications.

This work is organized as follows. Section 2 presents the governing equations, in continuous and discrete forms, of the 3-D and 1-D FSI models. Section 3 describes the fluid coupling equations and the numerical algorithms used to solve the heterogeneous network of FSI problems. The interface conditions for the solid part of the FSI problems are addressed in Section 4; more precisely, three different sets of boundary conditions are proposed to close the 3-D solid problem. These conditions are then used and tested in Section 5 on some benchmark problems, with the aim of analyzing and comparing the number of iterations and the impact of the spurious backward reflections at the coupling interfaces. In Section 6 the performance of the different numerical techniques are analyzed in the context of a physiological scenario. Finally, our conclusions are reported in Section 7.

2. Fluid-structure interaction models. As previously stated, the interaction between blood flow and arterial wall deformation (compression and dilatation) has to be taken into account to correctly reconstruct the behavior of the arterial pulse. In fact, blood flow is characterized by traveling waves, generated by the interaction between the fluid pressure and the wall deformation. In this section we recall the 3-D and the 1-D FSI models for the cardiovascular setting. For both models we then provide the numerical approximation techniques employed to solve the problems at the discrete level.

2.1. 3-D FSI model. In a geometrical multiscale setting, 3-D FSI models are used to simulate the hemodynamics in complex geometrical situations such as those occurring at bifurcations, aneurysms, and stenoses among others. In addition, when patient-specific analyses are aimed for, the correct characterization of the local arterial flow has to be carried out by using patient-specific data obtained from 3-D medical images.

2.1.1. Equations. Despite the complexity of the blood rheology, a Newtonian incompressible fluid is a suitable model for blood at the scale of larger arteries [16]. The arterial blood flow is therefore modeled with the incompressible Navier–Stokes equations in the case of a moving fluid domain, resulting in the so-called Arbitrary Lagrangian Eulerian (ALE) formulation [26]. This approach is motivated by the need of imposing the boundary conditions for the fluid equations on a moving domain.

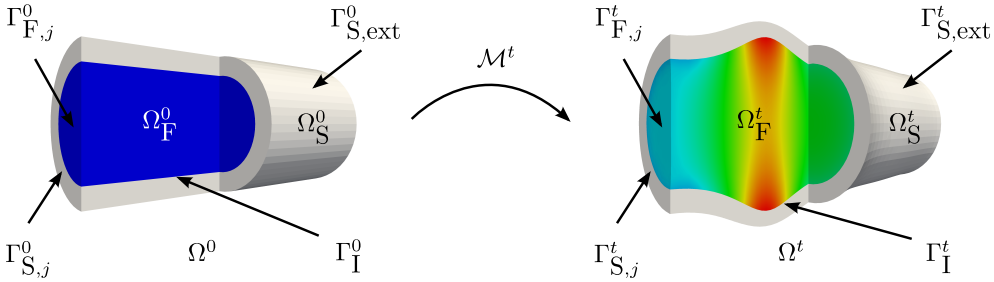

Figure 2.1: Reference and current configurations with ALE mapping. The color map in the scheme indicates the computed blood pressure field.

Let $\Omega^0 \subset \mathbb{R}^3$ be a 3-D bounded domain with Lipschitz continuous boundary $\partial\Omega^0$, where $\bar{\Omega}^0 = \bar{\Omega}^0_{\mathrm{F}} \cup \bar{\Omega}^0_{\mathrm{S}}$ denotes the reference configuration of the fluid-solid problem, being Ω^0_{F} and Ω^0_{S} the fluid and solid reference domains, respectively (see Figure 2.1). In addition, we denote by Γ^0_{I} the reference fluid-solid interface $\partial\Omega^0_{\mathrm{F}} \cap \partial\Omega^0_{\mathrm{S}}$. The ALE formulation leads to an arbitrary choice of the *geometrical problem*. In this work we describe the fluid domain displacement $\boldsymbol{d}_{\mathrm{F}}$ as harmonic extension of the solid displacement $\boldsymbol{d}_{\mathrm{S}}$ at the fluid-solid interface Γ^0_{I} to the interior of the fluid reference domain Ω^0_{F}, i.e.,

$$\begin{cases} -\boldsymbol{\Delta}\boldsymbol{d}_{\mathrm{F}} = \boldsymbol{0} & \text{in } \Omega^0_{\mathrm{F}}, \\ \boldsymbol{d}_{\mathrm{F}} - \boldsymbol{d}_{\mathrm{S}} = \boldsymbol{0} & \text{on } \Gamma^0_{\mathrm{I}}, \\ \boldsymbol{\nabla}\boldsymbol{d}_{\mathrm{F}} \cdot \boldsymbol{n}_{\mathrm{F}} = \boldsymbol{0} & \text{on } \partial\Omega^0_{\mathrm{F}} \backslash \Gamma^0_{\mathrm{I}}, \end{cases} \tag{2.1}$$

being $\boldsymbol{n}_{\mathrm{F}}$ the outgoing normal direction on the fluid domain boundary. The solid displacement $\boldsymbol{d}_{\mathrm{S}}$ changes with time, therefore the harmonic extension (2.1) defines the current configuration of the fluid domain Ω^t_{F}, which is parametrized by the ALE map

$$\begin{aligned} \mathcal{M}^t : \Omega^0_{\mathrm{F}} &\to \Omega^t_{\mathrm{F}} \subset \mathbb{R}^3 \\ \boldsymbol{x}^0 &\mapsto \mathcal{M}^t\left(\boldsymbol{x}^0\right) = \boldsymbol{x}^0 + \boldsymbol{d}_{\mathrm{F}}\left(\boldsymbol{x}^0\right), \end{aligned}$$

such that $\Omega^t_{\mathrm{F}} = \mathcal{M}^t\left(\Omega^0_{\mathrm{F}}\right)$, with $\boldsymbol{x}^0 \in \Omega^0_{\mathrm{F}}$ a fluid point in the reference configuration. This approach is very convenient in the description of deforming arteries since it allows to preserve the mesh topology during the simulations and just move its vertices.

The *fluid problem* consists of the incompressible Navier–Stokes equations written in the ALE formulation

$$\begin{cases} \rho_{\mathrm{F}}\left(\left.\dfrac{\partial \boldsymbol{u}_{\mathrm{F}}}{\partial t}\right|_{\boldsymbol{x}^0} + \left(\left(\boldsymbol{u}_{\mathrm{F}} - \boldsymbol{w}_{\mathrm{F}}\right) \cdot \boldsymbol{\nabla}\right)\boldsymbol{u}_{\mathrm{F}}\right) - \boldsymbol{\nabla} \cdot \sigma_{\mathrm{F}} = \boldsymbol{0} & \text{in } \Omega^t_{\mathrm{F}} \times (0,T], \\ \boldsymbol{\nabla} \cdot \boldsymbol{u}_{\mathrm{F}} = 0 & \text{in } \Omega^t_{\mathrm{F}} \times (0,T], \\ \boldsymbol{u}_{\mathrm{F}} - \overline{\boldsymbol{u}}_{\mathrm{F}} = \boldsymbol{0} & \text{in } \Omega^t_{\mathrm{F}} \times \{0\}, \end{cases} \tag{2.2}$$

where $(0,T]$ is the time interval, ρ_{F} the fluid density, $\sigma_{\mathrm{F}} = -p_{\mathrm{F}}\mathrm{I} + 2\mu_{\mathrm{F}}\,\epsilon_{\mathrm{F}}\left(\boldsymbol{u}_{\mathrm{F}}\right)$ the Cauchy stress tensor (with I the identity matrix), $\epsilon_{\mathrm{F}}\left(\boldsymbol{u}_{\mathrm{F}}\right) = \left(\boldsymbol{\nabla}\boldsymbol{u}_{\mathrm{F}} + \left(\boldsymbol{\nabla}\boldsymbol{u}_{\mathrm{F}}\right)^{\mathsf{T}}\right)/2$ the strain rate tensor, $\boldsymbol{u}_{\mathrm{F}}$ the fluid velocity vector field, $\overline{\boldsymbol{u}}_{\mathrm{F}}$ the initial fluid velocity vector field, p_{F} the fluid hydrostatic pressure, μ_{F} the given fluid dynamic viscosity, and, finally,

$$\boldsymbol{w}_{\mathrm{F}} = \left.\frac{\partial \mathcal{M}^t}{\partial t}\right|_{\boldsymbol{x}^0} = \left.\frac{\partial \boldsymbol{d}_{\mathrm{F}}}{\partial t}\right|_{\boldsymbol{x}^0} \tag{2.3}$$

is the fluid domain velocity. Problem (2.2) is closed by imposing an interface condition with the solid problem on Γ^0_{I} and inflow and outflow boundary conditions on $\Gamma^t_{\mathrm{F},j} \subset \partial\Omega^t_{\mathrm{F}} \backslash \Gamma^t_{\mathrm{I}}$, $j = 1, \ldots, n^{\Gamma}_{\mathrm{FS}}$. In a geometrical multiscale setting, some of these inflow/outflow boundaries are coupling interfaces with the nearby reduced dimensional model, where continuity equations are imposed, cf. Section 3. On the remaining boundaries we can impose given data, such as inlet/outlet time flow/velocity profiles. Note that since the number of boundaries n^{Γ}_{FS} is the same for both the fluid and the solid problems, we use the double subscript FS.

The *solid problem* is described in a purely Lagrangian frame of reference. A large variety of materials can be chosen for modeling the arterial wall. The mechanical response of the wall to a given strain is mainly due to the *elastin* and *collagen* components. The former one is responsible for the isotropic hyperelastic response, while the latter incorporates anisotropy and constitutive nonlinearity to the strain-stress relation; it is activated only when the strains reach a certain critical value and in certain directions (according to fiber orientation). In this regard, we consider a linear elastic model for the elastin and neglect the nonlinearities due to fiber orientation and activation. In addition, we assume a quasi-incompressible behavior for the arterial tissue and neglect its viscoelastic response. In fact, an equivalent viscoelastic effect is accounted for through proper boundary conditions acting over the external wall surface coming from a model of the surrounding tissues (see, for instance, [27]). As a result of these considerations, in this work we consider a linear elastic isotropic St. Venant–Kirchhoff model to describe the solid displacement

$$\begin{cases} \rho_{\mathrm{S}} \dfrac{\partial^2 \boldsymbol{d}_{\mathrm{S}}}{\partial t^2} - \boldsymbol{\nabla} \cdot \sigma_{\mathrm{S}} = \mathbf{0} & \text{in } \Omega_{\mathrm{S}}^0 \times (0,T], \\ \boldsymbol{d}_{\mathrm{S}} - \overline{\boldsymbol{d}}_{\mathrm{S}} = \mathbf{0} & \text{in } \Omega_{\mathrm{S}}^0 \times \{0\}, \\ \dfrac{\partial \boldsymbol{d}_{\mathrm{S}}}{\partial t} - \overline{\boldsymbol{v}}_{\mathrm{S}} = \mathbf{0} & \text{in } \Omega_{\mathrm{S}}^0 \times \{0\}, \end{cases} \tag{2.4}$$

where ρ_{S} is the solid density, $\sigma_{\mathrm{S}} = \lambda_{\mathrm{S}} \mathrm{tr}\left(\epsilon_{\mathrm{S}}\left(\boldsymbol{d}_{\mathrm{S}}\right)\right) \mathrm{I} + 2\mu_{\mathrm{S}} \epsilon_{\mathrm{S}}\left(\boldsymbol{d}_{\mathrm{S}}\right)$ the first Piola–Kirchhoff stress tensor, being $\epsilon_{\mathrm{S}}\left(\boldsymbol{d}_{\mathrm{S}}\right) = \left(\boldsymbol{\nabla} \boldsymbol{d}_{\mathrm{S}} + \left(\boldsymbol{\nabla} \boldsymbol{d}_{\mathrm{S}}\right)^{\mathsf{T}}\right)/2$, λ_{S} and μ_{S} are the first and second Lamé parameters, respectively, $\overline{\boldsymbol{d}}_{\mathrm{S}}$ is the initial solid displacement, and $\overline{\boldsymbol{v}}_{\mathrm{S}}$ the initial solid velocity. The St. Venant–Kirchhoff materials are usually characterized by the Young modulus E_{S} and the Poisson coefficient ν_{S}. The following relations hold between the two sets of coefficients

$$\lambda_{\mathrm{S}} = \frac{E_{\mathrm{S}} \nu_{\mathrm{S}}}{\left(1 - 2\nu_{\mathrm{S}}\right)\left(1 + \nu_{\mathrm{S}}\right)}, \qquad \mu_{\mathrm{S}} = \frac{E_{\mathrm{S}}}{2\left(1 + \nu_{\mathrm{S}}\right)}.$$

Problem (2.4) is closed by imposing an interface condition with the fluid problem on Γ_{I}^0 and a proper set of boundary conditions on $\partial\Omega_{\mathrm{S}}^0 \backslash \Gamma_{\mathrm{I}}^0$. On the solid external wall $\Gamma_{\mathrm{S,ext}}^0$ we can apply either a Neumann boundary condition, to account for a distributed pressure field, or a viscoelastic Robin boundary condition, to model the presence of the external tissues on the arteries. In turn, in a geometrical multiscale setting, the area of the n_{FS}^{Γ} inlet/outlet solid rings $\Gamma_{\mathrm{S},j}^0$, $j = 1, \ldots, n_{\mathrm{FS}}^{\Gamma}$, can be related to the one of the surrounding models; on the contrary, if there exists any uncoupled boundary interface, a different approach must be followed. We defer this discussion to Section 4.

2.1.2. Solution strategy for the FSI problem. The solution of the FSI problem can be obtained by using either a *modular* (segregated) or *non-modular* (monolithic) strategy. Depending on the choice of the boundary conditions applied to the fluid and solid domains, the former approach may lead to Dirichlet–Neumann [8, 28], Neumann–Dirichlet [29], Robin–Neumann [30], or Robin–Robin [31] approaches. In all the cases, the main drawback is that an additional subiteration algorithm is required to achieve strong coupling between the fluid and the solid problems. Therefore, to avoid fluid-solid subiterations, we use a non-modular strategy, where the fluid and the solid are treated as a single problem. The problem is tackled by using a parallel blockwise preconditioner, developed in [12, 24]. It is based on an inexact block factorization where each factor is indeed an algebraic additive Schwarz preconditioner.

The resulting global preconditioner has proven to be effective and scalable, since it can be split in different factors, each one addressing a single subproblem in a specific way.

Problems (2.2) and (2.4) are coupled through interface conditions on Γ_{I}^0, which comprise the continuity of the velocity field and that of the traction (the latter with the use of a Lagrange multiplier). The *interface problem* reads

$$\begin{cases} \boldsymbol{u}_{\mathrm{F}} \circ \mathcal{M}^t - \dfrac{\partial \boldsymbol{d}_{\mathrm{S}}}{\partial t} = \boldsymbol{0} & \text{on } \Gamma_{\mathrm{I}}^0 \times (0,T], \\ \sigma_{\mathrm{S}} \cdot \boldsymbol{n}_{\mathrm{S}} - \boldsymbol{\lambda}_{\Gamma_{\mathrm{I}}} = \boldsymbol{0} & \text{on } \Gamma_{\mathrm{I}}^0 \times (0,T], \\ \boldsymbol{\lambda}_{\Gamma_{\mathrm{I}}} - J_{\mathrm{S}} \mathrm{G}_{\mathrm{S}}^{-\mathsf{T}} \left(\sigma_{\mathrm{F}} \circ \mathcal{M}^t\right) \cdot \boldsymbol{n}_{\mathrm{S}} = \boldsymbol{0} & \text{on } \Gamma_{\mathrm{I}}^0 \times (0,T], \end{cases} \tag{2.5}$$

where $\boldsymbol{\lambda}_{\Gamma_{\mathrm{I}}}$ is the Lagrange multiplier, $\boldsymbol{n}_{\mathrm{S}}$ the outgoing normal direction applied to the solid domain, $\mathrm{G}_{\mathrm{S}} = \mathrm{I} + \boldsymbol{\nabla} \boldsymbol{d}_{\mathrm{S}}$ the solid deformation gradient, and $J_{\mathrm{S}} = \det\left(\mathrm{G}_{\mathrm{S}}\right)$. For the ease of writing, let us formally denote problems (2.1), (2.2), (2.4), and (2.5) in their weak form as $\mathbf{G}$, $\mathbf{F}$, $\mathbf{S}$, and $\mathbf{I}$, respectively. This allows us to write the global variational formulation of the FSI problem in a compact form as follows: find $(\boldsymbol{u}_{\mathrm{F}}, p_{\mathrm{F}}) \in \boldsymbol{\mathcal{V}}_{\mathrm{F}}$, $\boldsymbol{d}_{\mathrm{S}} \in \boldsymbol{\mathcal{V}}_{\mathrm{S}}$, $\boldsymbol{\lambda}_{\Gamma_{\mathrm{I}}} \in \boldsymbol{\mathcal{V}}_{\mathrm{I}}$ and $\boldsymbol{d}_{\mathrm{F}} \in \boldsymbol{\mathcal{V}}_{\mathrm{G}}$ such that

$$\begin{cases} \mathbf{F}((\boldsymbol{u}_{\mathrm{F}}, p_{\mathrm{F}}, \boldsymbol{\lambda}_{\Gamma_{\mathrm{I}}}, \boldsymbol{d}_{\mathrm{F}}), (\boldsymbol{u}_{\mathrm{F}}^*, p_{\mathrm{F}}^*)) = \boldsymbol{0} & \forall (\boldsymbol{u}_{\mathrm{F}}^*, p_{\mathrm{F}}^*) \in \boldsymbol{\mathcal{V}}_{\mathrm{F}}^*, \\ \mathbf{S}((\boldsymbol{d}_{\mathrm{S}}, \boldsymbol{\lambda}_{\Gamma_{\mathrm{I}}}), \boldsymbol{d}_{\mathrm{S}}^*) = \boldsymbol{0} & \forall \boldsymbol{d}_{\mathrm{S}}^* \in \boldsymbol{\mathcal{V}}_{\mathrm{S}}^*, \\ \mathbf{I}((\boldsymbol{u}_{\mathrm{F}}, \boldsymbol{d}_{\mathrm{S}}), \boldsymbol{\lambda}_{\Gamma_{\mathrm{I}}}^*) = \boldsymbol{0} & \forall \boldsymbol{\lambda}_{\Gamma_{\mathrm{I}}}^* \in \boldsymbol{\mathcal{V}}_{\mathrm{I}}^*, \\ \mathbf{G}((\boldsymbol{d}_{\mathrm{S}}, \boldsymbol{d}_{\mathrm{F}}), \boldsymbol{d}_{\mathrm{F}}^*) = \boldsymbol{0} & \forall \boldsymbol{d}_{\mathrm{F}}^* \in \boldsymbol{\mathcal{V}}_{\mathrm{G}}^*, \end{cases} \tag{2.6}$$

where $\boldsymbol{\mathcal{V}}_{\mathrm{F}}$, $\boldsymbol{\mathcal{V}}_{\mathrm{S}}$, $\boldsymbol{\mathcal{V}}_{\mathrm{I}}$, and $\boldsymbol{\mathcal{V}}_{\mathrm{G}}$ are proper linear manifolds including the corresponding essential conditions according to the boundary data; the superscript $*$ identifies test functions and spaces.

2.1.3. Numerical approximation. The fluid problem is discretized in space by a $\mathbb{P}1$–$\mathbb{P}1$ finite element method, stabilized by an interior penalty technique [32]. The solid and the geometric problems are discretized in space by $\mathbb{P}1$ finite elements. These discretizations show a first order convergence in space. For the sake of simplicity, in the following discrete forms we omit the subscript h which refers to the spatial discretization. A large variety of time discretizations for the incompressible Navier–Stokes equations on moving domains can be found in the literature, depending on the target application. In this work we use a first order Euler scheme. Regarding the structural problem, we use an explicit second order mid-point scheme, which can be interpreted as a Newmark scheme with a particular choice of the coefficients. The extension of the proposed methodology to other time discretizations is straightforward and it is not a matter of concern here. The global time interval $[0,T]$ is split into several uniform subintervals $[t^n, t^{n+1}]$, $n = 0, 1, 2, \ldots$, such that $t^n = n\Delta t$, Δt being the time step.

Problem (2.6) is highly nonlinear due to the Navier–Stokes convective term and to the displacement of the fluid domain. Following the approach devised in [24], we use different time discretization strategies to address such nonlinearities. In both cases, the solution of the non-modular FSI problem is performed by using the Newton method [12, 24]. Several approximations of the corresponding Jacobian matrix by finite difference methods are reviewed in the literature (see, for instance, [7, 9, 11]). However, these schemes may lead to a substantial increase of the number of iterations required for the convergence to the solution of the FSI problem. For this reason, in

this work we compute the Jacobian blocks by an analytic formulation, which takes into account the shape derivatives, i.e., the cross derivatives of the fluid problem with respect to the domain motion. For a detailed description, including the derivation of the Jacobian blocks, see [12, Section 3.4] and [33].

Let $\boldsymbol{u}_{\mathrm{FSI}}$ be the vector of unknowns of the FSI problem. The p-th iteration of the Newton method reads

$$\boldsymbol{u}_{\mathrm{FSI}}^{p+1} = \boldsymbol{u}_{\mathrm{FSI}}^{p} + \delta\boldsymbol{u}_{\mathrm{FSI}}^{p}, \tag{2.7}$$

where the update $\delta\boldsymbol{u}_{\mathrm{FSI}}^{p}$ is computed by solving

$$\mathcal{J}_{\mathrm{FSI}}\left(\boldsymbol{u}_{\mathrm{FSI}}^{p}\right)\delta\boldsymbol{u}_{\mathrm{FSI}}^{p} = -\boldsymbol{\mathcal{R}}_{\mathrm{FSI}}\left(\boldsymbol{u}_{\mathrm{FSI}}^{p}\right). \tag{2.8}$$

This approach requires the computation of the Jacobian matrix $\mathcal{J}_{\mathrm{FSI}}\left(\boldsymbol{u}_{\mathrm{FSI}}^{p}\right)$ and the evaluation of the residuals vector $\boldsymbol{\mathcal{R}}_{\mathrm{FSI}}\left(\boldsymbol{u}_{\mathrm{FSI}}^{p}\right)$ at each p-th iteration. The specific expression of these two elements depends on the chosen time discretization strategy.

Fully implicit (FI) time discretization. The geometric and convective terms in the equations are considered implicitly, such that the unknowns vector is $\boldsymbol{u}_{\mathrm{FSI}} = \left(\boldsymbol{y}_{\mathrm{F}}^{\mathsf{T}}, \boldsymbol{d}_{\mathrm{S}}^{\mathsf{T}}, \boldsymbol{\lambda}_{\Gamma_{\mathrm{I}}}^{\mathsf{T}}, \boldsymbol{d}_{\mathrm{F}}^{\mathsf{T}}\right)^{\mathsf{T}}$, being $\boldsymbol{y}_{\mathrm{F}} = \left(\boldsymbol{u}_{\mathrm{F}}^{\mathsf{T}}, p_{\mathrm{F}}^{\mathsf{T}}\right)^{\mathsf{T}}$. The FI formulation reads: given $\boldsymbol{u}_{\mathrm{FSI}}^{n}$, find $\boldsymbol{u}_{\mathrm{FSI}}^{n+1}$ such that

$$\mathrm{A}_{\mathrm{FSI}}^{n+1}\boldsymbol{u}_{\mathrm{FSI}}^{n+1} = \boldsymbol{b}_{\mathrm{FSI}}^{n+1},$$

being

$$\mathrm{A}_{\mathrm{FSI}}^{n+1} = \left[\begin{array}{cc|cc|c|cc}
\mathrm{F}_{\mathrm{FF}}\left(\boldsymbol{y}_{\mathrm{F}}^{n+1}, \boldsymbol{d}_{\mathrm{F}}^{n+1}\right) & \mathrm{F}_{\mathrm{F}\Gamma_{\mathrm{I}}}\left(\boldsymbol{y}_{\mathrm{F}}^{n+1}, \boldsymbol{d}_{\mathrm{F}}^{n+1}\right) & 0 & 0 & 0 & 0 & 0 \\
\mathrm{F}_{\Gamma_{\mathrm{I}}\mathrm{F}}\left(\boldsymbol{y}_{\mathrm{F}}^{n+1}, \boldsymbol{d}_{\mathrm{F}}^{n+1}\right) & \mathrm{F}_{\Gamma_{\mathrm{I}}\Gamma_{\mathrm{I}}}\left(\boldsymbol{y}_{\mathrm{F}}^{n+1}, \boldsymbol{d}_{\mathrm{F}}^{n+1}\right) & 0 & 0 & \Lambda_{\mathrm{F}} & 0 & 0 \\
\hline
0 & 0 & \mathrm{S}_{\mathrm{SS}} & \mathrm{S}_{\mathrm{S}\Gamma_{\mathrm{I}}} & 0 & 0 & 0 \\
0 & 0 & \mathrm{S}_{\Gamma_{\mathrm{I}}\mathrm{S}} & \mathrm{S}_{\Gamma_{\mathrm{I}}\Gamma_{\mathrm{I}}} & -\mathrm{I} & 0 & 0 \\
\hline
0 & \Lambda_{\mathrm{F}}^{\mathsf{T}} & 0 & -\mathrm{I}/\Delta t & 0 & 0 & 0 \\
\hline
0 & 0 & 0 & 0 & 0 & \mathrm{G}_{\mathrm{FF}} & \mathrm{G}_{\mathrm{F}\Gamma_{\mathrm{I}}} \\
0 & 0 & 0 & -\mathrm{I} & 0 & 0 & \mathrm{I}
\end{array}\right],$$

and

$$\boldsymbol{u}_{\mathrm{FSI}}^{n+1} = \left(\begin{array}{c}
\boldsymbol{y}_{\mathrm{FF}}^{n+1} \\
\hline
\boldsymbol{y}_{\mathrm{F}\Gamma_{\mathrm{I}}}^{n+1} \\
\hline
\boldsymbol{d}_{\mathrm{SS}}^{n+1} \\
\hline
\boldsymbol{d}_{\mathrm{S}\Gamma_{\mathrm{I}}}^{n+1} \\
\hline
\boldsymbol{\lambda}_{\Gamma_{\mathrm{I}}}^{n+1} \\
\hline
\boldsymbol{d}_{\mathrm{FF}}^{n+1} \\
\boldsymbol{d}_{\mathrm{F}\Gamma_{\mathrm{I}}}^{n+1}
\end{array}\right), \qquad \boldsymbol{b}_{\mathrm{FSI}}^{n+1} = \left(\begin{array}{c}
\boldsymbol{b}_{\mathrm{FF}}\left(\boldsymbol{d}_{\mathrm{F}}^{n+1}\right) \\
\hline
\boldsymbol{b}_{\mathrm{F}\Gamma_{\mathrm{I}}}\left(\boldsymbol{d}_{\mathrm{F}}^{n+1}\right) \\
\hline
\boldsymbol{b}_{\mathrm{SS}} \\
\hline
\boldsymbol{b}_{\mathrm{S}\Gamma_{\mathrm{I}}} \\
\hline
-\boldsymbol{d}_{\mathrm{S}\Gamma_{\mathrm{I}}}^{n}/\Delta t \\
\hline
\boldsymbol{0} \\
\boldsymbol{0}
\end{array}\right),$$

where in the algebraic form, for the sake of clarity, we distinguish between the degrees of freedom lying on the fluid-solid interface (adding the subscript Γ_{I} to the blocks) and those that are internal to the domains Ω_{F}^{t} and Ω_{S}^{0} (for which we keep the same subscripts as for the continuous case). In particular, $\boldsymbol{y}_{\mathrm{F}} = \left(\boldsymbol{y}_{\mathrm{FF}}^{\mathsf{T}}, \boldsymbol{y}_{\mathrm{F}\Gamma_{\mathrm{I}}}^{\mathsf{T}}\right)^{\mathsf{T}}$, $\boldsymbol{d}_{\mathrm{S}} = \left(\boldsymbol{d}_{\mathrm{SS}}^{\mathsf{T}}, \boldsymbol{d}_{\mathrm{S}\Gamma_{\mathrm{I}}}^{\mathsf{T}}\right)^{\mathsf{T}}$, and $\boldsymbol{d}_{\mathrm{F}} = \left(\boldsymbol{d}_{\mathrm{FF}}^{\mathsf{T}}, \boldsymbol{d}_{\mathrm{F}\Gamma_{\mathrm{I}}}^{\mathsf{T}}\right)^{\mathsf{T}}$. Blocks (1,1), (2,2), and (4,4) represent the

discrete fluid, solid, and geometric problems, respectively. The off-diagonal entries enforce the coupling conditions between the three fields. The rectangular block matrix Λ_{F} coincides with $[\mathrm{I}, 0]^{\mathsf{T}}$, such that it selects the fluid velocity degrees of freedom of $\boldsymbol{y}_{\mathrm{F}\Gamma_{\mathrm{I}}}$ to apply the fluid-solid interface conditions. Note that in this discrete formulation we suppose a first order time discretization of the velocity continuity coupling condition. The nonlinearities, i.e., the dependence of the fluid blocks from the fluid displacement and from the fluid velocity and pressure fields, are explicitly indicated in the matrix entries. The fluid and solid right-hand sides including the terms generated by the time discretization of the momentum conservation equations are denoted by $\boldsymbol{b}_{\mathrm{F}} = (\boldsymbol{b}_{\mathrm{FF}}^{\mathsf{T}}, \boldsymbol{b}_{\mathrm{F}\Gamma_{\mathrm{I}}}^{\mathsf{T}})^{\mathsf{T}}$ and $\boldsymbol{b}_{\mathrm{S}} = (\boldsymbol{b}_{\mathrm{SS}}^{\mathsf{T}}, \boldsymbol{b}_{\mathrm{S}\Gamma_{\mathrm{I}}}^{\mathsf{T}})^{\mathsf{T}}$, respectively. We remark that, due to the implicit formulation adopted for the fluid domain, also the fluid right-hand side depends on the fluid domain displacement. The residual of the Newton method is defined as $\boldsymbol{\mathcal{R}}_{\mathrm{FSI}} = \mathrm{A}_{\mathrm{FSI}}\boldsymbol{u}_{\mathrm{FSI}} - \boldsymbol{b}_{\mathrm{FSI}}$, while the Jacobian matrix $\mathcal{J}_{\mathrm{FSI}}(\boldsymbol{u}_{\mathrm{FSI}})$ assumes the form

$$
\left[\begin{array}{cc|cc|c|cc}
\mathrm{D}_{\boldsymbol{y}_{\mathrm{FF}}}\mathrm{F}_{\mathrm{F}} & \mathrm{D}_{\boldsymbol{y}_{\mathrm{F}\Gamma_{\mathrm{I}}}}\mathrm{F}_{\mathrm{F}} & 0 & 0 & 0 & \mathrm{D}_{\boldsymbol{d}_{\mathrm{FF}}}(\mathrm{F}_{\mathrm{F}} + \boldsymbol{b}_{\mathrm{F}}) & \mathrm{D}_{\boldsymbol{d}_{\mathrm{F}\Gamma_{\mathrm{I}}}}(\mathrm{F}_{\mathrm{F}} + \boldsymbol{b}_{\mathrm{F}}) \\
\mathrm{D}_{\boldsymbol{y}_{\mathrm{FF}}}\mathrm{F}_{\Gamma_{\mathrm{I}}} & \mathrm{D}_{\boldsymbol{y}_{\mathrm{F}\Gamma_{\mathrm{I}}}}\mathrm{F}_{\Gamma_{\mathrm{I}}} & 0 & 0 & \Lambda_{\mathrm{F}} & \mathrm{D}_{\boldsymbol{d}_{\mathrm{FF}}}(\mathrm{F}_{\Gamma_{\mathrm{I}}} + \boldsymbol{b}_{\Gamma_{\mathrm{I}}}) & \mathrm{D}_{\boldsymbol{d}_{\mathrm{F}\Gamma_{\mathrm{I}}}}(\mathrm{F}_{\Gamma_{\mathrm{I}}} + \boldsymbol{b}_{\Gamma_{\mathrm{I}}}) \\
\hline
0 & 0 & \mathrm{S}_{\mathrm{SS}} & \mathrm{S}_{\mathrm{S}\Gamma_{\mathrm{I}}} & 0 & 0 & 0 \\
0 & 0 & \mathrm{S}_{\Gamma_{\mathrm{I}}\mathrm{S}} & \mathrm{S}_{\Gamma_{\mathrm{I}}\Gamma_{\mathrm{I}}} & -\mathrm{I} & 0 & 0 \\
\hline
0 & \Lambda_{\mathrm{F}}^{\mathsf{T}} & 0 & -\mathrm{I}/\Delta t & 0 & 0 & 0 \\
\hline
0 & 0 & 0 & 0 & 0 & \mathrm{G}_{\mathrm{FF}} & \mathrm{G}_{\mathrm{F}\Gamma_{\mathrm{I}}} \\
0 & 0 & 0 & -\mathrm{I} & 0 & 0 & \mathrm{I}
\end{array}\right].
$$

Note that in the Jacobian matrix we have used the abridged notations $\mathrm{D}_{\mathbf{x}}\mathrm{F}_{\mathrm{F}} = \mathrm{D}_{\mathbf{x}}\mathrm{F}_{\mathrm{FF}} + \mathrm{D}_{\mathbf{x}}\mathrm{F}_{\mathrm{F}\Gamma_{\mathrm{I}}}$, $\mathrm{D}_{\mathbf{x}}\mathrm{F}_{\Gamma_{\mathrm{I}}} = \mathrm{D}_{\mathbf{x}}\mathrm{F}_{\Gamma_{\mathrm{I}}\mathrm{F}} + \mathrm{D}_{\mathbf{x}}\mathrm{F}_{\Gamma_{\mathrm{I}}\Gamma_{\mathrm{I}}}$, $\mathrm{D}_{\mathbf{x}}\boldsymbol{b}_{\mathrm{F}} = \mathrm{D}_{\mathbf{x}}\boldsymbol{b}_{\mathrm{FF}} + \mathrm{D}_{\mathbf{x}}\boldsymbol{b}_{\mathrm{F}\Gamma_{\mathrm{I}}}$, and $\mathrm{D}_{\mathbf{x}}\boldsymbol{b}_{\Gamma_{\mathrm{I}}} = \mathrm{D}_{\mathbf{x}}\boldsymbol{b}_{\Gamma_{\mathrm{I}}\mathrm{F}} + \mathrm{D}_{\mathbf{x}}\boldsymbol{b}_{\Gamma_{\mathrm{I}}\Gamma_{\mathrm{I}}}$, being $\mathrm{D}_{\mathbf{x}}$ the total derivative of a given functional with respect to a variable $\mathbf{x}$.

Geometric convective explicit (GCE) time discretization. We define appropriate extrapolations $\boldsymbol{d}_{\mathrm{S}\Gamma_{\mathrm{I}}}^{\diamond}$ and $\boldsymbol{u}_{\mathrm{F}}^{\diamond}$ of the geometric and convective terms, respectively. More precisely, by choosing the simplest approximation, i.e., $\boldsymbol{d}_{\mathrm{S}\Gamma_{\mathrm{I}}}^{\diamond} = \boldsymbol{d}_{\mathrm{S}\Gamma_{\mathrm{I}}}^{n}$ and $\boldsymbol{u}_{\mathrm{F}}^{\diamond} = \boldsymbol{u}_{\mathrm{F}}^{n}$, we split the geometric part of the problem from the fluid-solid one. Hence, at each time step, first we compute the fluid displacement $\boldsymbol{d}_{\mathrm{F}}^{n+1}$ by solving the linear system associated to the geometric problem, i.e.,

$$
\begin{bmatrix} \mathrm{G}_{\mathrm{FF}} & \mathrm{G}_{\mathrm{F}\Gamma_{\mathrm{I}}} \\ 0 & \mathrm{I} \end{bmatrix} \begin{pmatrix} \boldsymbol{d}_{\mathrm{FF}}^{n+1} \\ \boldsymbol{d}_{\mathrm{F}\Gamma_{\mathrm{I}}}^{n+1} \end{pmatrix} - \begin{pmatrix} \mathbf{0} \\ \boldsymbol{d}_{\mathrm{S}\Gamma_{\mathrm{I}}}^{n} \end{pmatrix} = \mathbf{0}, \tag{2.9}
$$

and we move the fluid mesh accordingly. Then, by using the resulting fluid domain velocity $\boldsymbol{w}_{\mathrm{F}}^{n+1}$, we replace the convective term in the fluid momentum equation by $\left(\left(\boldsymbol{u}_{\mathrm{F}}^{\diamond} - \boldsymbol{w}_{\mathrm{F}}^{n+1}\right) \cdot \boldsymbol{\nabla}\right) \boldsymbol{u}_{\mathrm{F}}^{n+1}$. The unknowns vector is reduced to $\boldsymbol{u}_{\mathrm{FSI}} = (\boldsymbol{y}_{\mathrm{F}}^{\mathsf{T}}, \boldsymbol{d}_{\mathrm{S}}^{\mathsf{T}}, \boldsymbol{\lambda}_{\Gamma_{\mathrm{I}}}^{\mathsf{T}})^{\mathsf{T}}$, and the second step reads: given $\boldsymbol{u}_{\mathrm{FSI}}^{n}$, find $\boldsymbol{u}_{\mathrm{FSI}}^{n+1}$ such that

$$
\mathrm{A}_{\mathrm{FSI}}^{n+1}\boldsymbol{u}_{\mathrm{FSI}}^{n+1} = \boldsymbol{b}_{\mathrm{FSI}}^{n+1},
$$

being

$$\mathrm{A}_{\mathrm{FSI}}^{n+1} = \left[\begin{array}{cc|cc|c} \mathrm{F}_{\mathrm{FF}} & \mathrm{F}_{\mathrm{F}\Gamma_{\mathrm{I}}} & 0 & 0 & 0 \\ \mathrm{F}_{\Gamma_{\mathrm{I}}\mathrm{F}} & \mathrm{F}_{\Gamma_{\mathrm{I}}\Gamma_{\mathrm{I}}} & 0 & 0 & \Lambda_{\mathrm{F}} \\ \hline 0 & 0 & \mathrm{S}_{\mathrm{SS}} & \mathrm{S}_{\mathrm{S}\Gamma_{\mathrm{I}}} & 0 \\ 0 & 0 & \mathrm{S}_{\Gamma_{\mathrm{I}}\mathrm{S}} & \mathrm{S}_{\Gamma_{\mathrm{I}}\Gamma_{\mathrm{I}}} & -\mathrm{I} \\ \hline 0 & \Lambda_{\mathrm{F}}^{\mathrm{T}} & 0 & -\mathrm{I}/\Delta t & 0 \end{array}\right]$$

and

$$\boldsymbol{u}_{\mathrm{FSI}}^{n+1} = \left(\begin{array}{c} \boldsymbol{y}_{\mathrm{FF}}^{n+1} \\ \hline \boldsymbol{y}_{\mathrm{F}\Gamma_{\mathrm{I}}}^{n+1} \\ \hline \boldsymbol{d}_{\mathrm{SS}}^{n+1} \\ \boldsymbol{d}_{\mathrm{S}\Gamma_{\mathrm{I}}}^{n+1} \\ \hline \boldsymbol{\lambda}_{\Gamma_{\mathrm{I}}}^{n+1} \end{array}\right), \qquad \boldsymbol{b}_{\mathrm{FSI}}^{n+1} = \left(\begin{array}{c} \boldsymbol{b}_{\mathrm{FF}} \\ \hline \boldsymbol{b}_{\mathrm{F}\Gamma_{\mathrm{I}}} \\ \hline \boldsymbol{b}_{\mathrm{SS}} \\ \boldsymbol{b}_{\mathrm{S}\Gamma_{\mathrm{I}}} \\ \hline -\boldsymbol{d}_{\mathrm{S}\Gamma_{\mathrm{I}}}^{n}/\Delta t \end{array}\right).$$

As for the FI time discretization, the residual of the Newton method is defined as $\boldsymbol{\mathcal{R}}_{\mathrm{FSI}} = \mathrm{A}_{\mathrm{FSI}}\boldsymbol{u}_{\mathrm{FSI}} - \boldsymbol{b}_{\mathrm{FSI}}$. In addition, since the problem is linear, the Jacobian is equal to the system matrix and the Newton method converges in one iteration.

2.2. 1-D FSI model. In a geometrical multiscale setting, the global arterial circulation can be modeled by a network of 1-D FSI segments, each one characterized by a circular cross-section (eventually narrowed along the axial direction) and a viscoelastic arterial wall (see, for instance, [2, 13, 14]). Despite the fact that the 1-D FSI model provides a simple axial symmetric representation of the blood flow, it has proven to be able to accurately describe the behavior of the principal physiological quantities in a mean sense with respect to the transversal area of the vessel.

2.2.1. Equations. The 1-D FSI model is derived from the incompressible Navier–Stokes equations by making some simplifying assumptions and integrating over the cross-section of the artery $\mathrm{S}(t,z)$, being $t \in (0,T]$ the time and $z \in [0,L]$ the axial coordinate, with L the length of the vessel. The fluid equations are coupled with a structural model for the vessel wall. The vessel is assumed to be axisymmetric and only radial displacements are considered. The pressure is assumed to be constant on each transversal section, while a Womersley axial velocity profile is imposed through a given power-law relation [14, 34]. The resulting state variables are

$$A(t,z) = \int_{\mathrm{S}(t,z)} \mathrm{dS}, \qquad Q(t,z) = \int_{\mathrm{S}(t,z)} u_{z\mathrm{F}}(t,z)\,\mathrm{dS}, \qquad P(t,z) = \frac{1}{A(t,z)} \int_{\mathrm{S}(t,z)} p_{\mathrm{F}}(t,z)\,\mathrm{dS},$$

where A is the cross-sectional area, Q is the volumetric flow rate, $u_{z\mathrm{F}}$ is the fluid axial velocity, and P is the average pressure. A derivation of the 1-D FSI model can be found in [35]. The resulting governing equations for continuity of mass and momentum are

$$\begin{cases} \dfrac{\partial A}{\partial t} + \dfrac{\partial Q}{\partial z} = 0 & \text{in } (0,L)\times(0,T], \\ \dfrac{\partial Q}{\partial t} + \dfrac{\partial}{\partial z}\left(\alpha_{\mathrm{F}}\dfrac{Q^2}{A}\right) + \dfrac{A}{\rho_{\mathrm{F}}}\dfrac{\partial P}{\partial z} + \kappa_{\mathrm{F}}\dfrac{Q}{A} = 0 & \text{in } (0,L)\times(0,T], \\ A - \overline{A} = 0, \quad Q - \overline{Q} = 0 & \text{in } (0,L)\times\{0\}, \end{cases} \tag{2.10}$$

where α_F and κ_F are the Coriolis and friction coefficients, respectively, whose definitions are given in [14]. In (2.10) we also provide the initial values for the area $\overline{A}$ and for the volumetric flow rate $\overline{Q}$.

The fluid problem (2.10) is coupled with the 1-D structural model through the pressure-area relation, which may account for several terms [2]. In this work we consider the elastic and viscoelastic responses of the vessel wall, since the other terms provide a negligible contribution in the cardiovascular 1-D modeling context (see, for instance, [13, 14, 23]),

$$P = \psi(A) = P_{\text{ext}} + \beta_S \left(\sqrt{\frac{A}{A^0}} - 1 \right) + \gamma_S \left(\frac{1}{A\sqrt{A}} \frac{\partial A}{\partial t} \right) \qquad \text{in } (0, L) \times (0, T], \quad (2.11)$$

being P_{ext} a reference external pressure (i.e., the pressure exerted by the tissues over the external wall), A^0 the reference value for the vessel area, and

$$\beta_S = \sqrt{\frac{\pi}{A^0}} \frac{h_S E_S}{1 - \nu_S^2}, \qquad \gamma_S = \frac{T_S \tan \phi_S}{4\sqrt{\pi}} \frac{h_S E_S}{1 - \nu_S^2},$$

where h_S is the wall thickness, T_S the wave characteristic time, and ϕ_S the viscoelastic angle. In cardiovascular applications T_S is usually taken equal to the systolic period, while the viscoelastic angle is a parameter which provides a measure of the relative magnitude of the parietal viscosity force to the elastic one. Note that the initial condition for the average pressure can be computed by plugging $\overline{A}$ and its time derivative in (2.11). The 1-D FSI problem is finally closed by providing a proper set of boundary conditions on both sides of the model. As for the 3-D counterpart, these conditions can be either given data (for instance expressing either a time-dependent heart flow [13] or a terminal absorbing condition [1]) or coupling conditions relating the 1-D problem with the surrounding models. We postpone the discussion of the latter case to Section 3. For further details about the 1-D FSI model equations see [14].

2.2.2. Numerical approximation. By plugging (2.11) into (2.10), we get a closed system of differential equations. On the one hand, the elastic component of the pressure-area relation is an algebraic expression and can be easily manipulated. On the other hand, the viscoelastic term depends on the temporal derivative of the area and requires a special treatment.

In the literature, several approaches have been proposed for the numerical approximation of the 1-D FSI problem, ranging from explicit discontinuous Galerkin [1], implicit finite difference [13], or implicit finite element [23] methods. Following [2, 14, 36], in this work we use an operator splitting technique based on an explicit second order Taylor–Galerkin discretization, where the volumetric flow rate is split into two components such that $Q = \widehat{Q} + \widetilde{Q}$, being $\widehat{Q}$ the solution of the pure elastic problem and $\widetilde{Q}$ the viscoelastic correction. On each time subinterval $[t^n, t^{n+1}]$, we solve the 1-D FSI problem by performing two steps.

1st step (elastic response). By removing the viscoelastic component from the formulation we can write the closed system of equations in the classical conservative form as

$$\frac{\partial \widehat{\boldsymbol{U}}}{\partial t} + \frac{\partial \boldsymbol{F}(\boldsymbol{U})}{\partial z} + \boldsymbol{S}(\boldsymbol{U}) = \boldsymbol{0} \qquad \text{in } (0, L) \times (0, T], \quad (2.12)$$

where $\boldsymbol{U} = [A, Q]^\intercal$ and $\widehat{\boldsymbol{U}} = [A, \widehat{Q}]^\intercal$ are the total and elastic conservative variables, respectively, $\boldsymbol{F} = [Q, F_2]^\intercal$ the corresponding fluxes, and $\boldsymbol{S} = [0, S_2]^\intercal$ accounts for the friction and the non-uniformity of the geometry and the material (see [14] for the detailed expression of F_2 and S_2). The flux $\boldsymbol{F}$ is algebraic, since it includes only the elastic part of (2.11). From (2.12) the Taylor–Galerkin formulation reads: given $\boldsymbol{U}_h^n = [A_h^n, Q_h^n]^\intercal$, find $\widehat{\boldsymbol{U}}_h^{n+1} = [A_h^{n+1}, \widehat{Q}_h^{n+1}]^\intercal \in \mathcal{V}_A \otimes \mathcal{V}_{\widehat{Q}}$ such that

$$(\widehat{\boldsymbol{U}}_h^{n+1}, \varphi_h) = (\widehat{\boldsymbol{U}}_h^{n}, \varphi_h) + \Delta t \left[\boldsymbol{F}\left(\boldsymbol{U}_h^n\right) - \frac{\Delta t}{2} \frac{\partial \boldsymbol{F}\left(\boldsymbol{U}_h^n\right)}{\partial \boldsymbol{U}} \left(\boldsymbol{S}\left(\boldsymbol{U}_h^n\right) + \frac{\partial \boldsymbol{F}\left(\boldsymbol{U}_h^n\right)}{\partial z} \right), \frac{\partial \varphi_h}{\partial z} \right]$$
$$-\Delta t \left[\boldsymbol{S}\left(\boldsymbol{U}_h^n\right) - \frac{\Delta t}{2} \frac{\partial \boldsymbol{S}\left(\boldsymbol{U}_h^n\right)}{\partial \boldsymbol{U}} \left(\boldsymbol{S}\left(\boldsymbol{U}_h^n\right) + \frac{\partial \boldsymbol{F}\left(\boldsymbol{U}_h^n\right)}{\partial z} \right), \varphi_h \right], \quad \forall \varphi_h \in \mathcal{V}_A^* \otimes \mathcal{V}_{\widehat{Q}}^*, \tag{2.13}$$

being $\boldsymbol{U}_h$ the discrete counterpart of $\boldsymbol{U}$, $\mathcal{V}_A$ and $\mathcal{V}_{\widehat{Q}}$ two sets of piecewise linear finite element functions with adequate boundary conditions and $\mathcal{V}_A^*$ and $\mathcal{V}_{\widehat{Q}}^*$ the associated linear spaces of admissible variations. The discrete problem is finally closed by introducing two compatibility conditions [14].

The main advantage of this approach resides in its very low computational cost in view of the explicit nature of the numerical method (2.13). Moreover, the solution of the problem for the area (mass conservation equation) is decoupled from the one for the volumetric flow rate (momentum conservation equation). However, the explicit time discretization entails a limitation on the time step due to the CFL condition, which in this case reads [37]

$$\frac{\Delta t}{h} < \frac{\sqrt{3}}{3}.$$

This is, as a matter of fact, a central issue when coupling 1-D and 3-D FSI problems, as we will see in Section 3.3.2.

2nd step (viscoelastic correction). By using the mass conservation equation, we remove the time dependence from the viscoelastic wall term. The resulting problem is

$$\frac{1}{A}\frac{\partial \widetilde{Q}}{\partial t} - \frac{\partial}{\partial z}\left(\frac{\gamma_{\mathrm{S}}}{\rho_{\mathrm{F}} A^{3/2}} \frac{\partial Q}{\partial z} \right) = 0 \qquad \text{in } (0, L) \times (0, T],$$

which is closed by a proper set of homogeneous boundary conditions for $\widetilde{Q}$. The corresponding finite element formulation reads: given $(A_h^{n+1}, \widehat{Q}_h^{n+1}) \in \mathcal{V}_A \otimes \mathcal{V}_{\widehat{Q}}$, find $\widetilde{Q}_h^{n+1} \in \mathcal{V}_{\widetilde{Q}}$ such that

$$\left(\frac{\widetilde{Q}_h^{n+1}}{A_h^{n+1}}, \varphi_h \right) + \Delta t \left(\frac{\gamma_{\mathrm{S}}}{\rho_{\mathrm{F}} \left(A_h^{n+1}\right)^{3/2}} \frac{\partial \widetilde{Q}_h^{n+1}}{\partial z}, \frac{\partial \varphi_h}{\partial z} \right) = \left(\frac{\widetilde{Q}_h^{n}}{A_h^{n+1}}, \varphi_h \right)$$
$$-\Delta t \left(\frac{\gamma_{\mathrm{S}}}{\rho_{\mathrm{F}} \left(A_h^{n+1}\right)^{3/2}} \frac{\partial \widehat{Q}_h^{n+1}}{\partial z}, \frac{\partial \varphi_h}{\partial z} \right) + \Delta t \left[\frac{\gamma_{\mathrm{S}}}{\rho_{\mathrm{F}} \left(A_h^{n+1}\right)^{3/2}} \frac{\partial \widehat{Q}_h^{n+1}}{\partial z} \varphi_h \right]_0^L, \quad \forall \varphi_h \in \mathcal{V}_{\widetilde{Q}}^*, \tag{2.14}$$

where $\mathcal{V}_{\widetilde{Q}}$ is a set of piecewise linear finite element functions with adequate boundary conditions and $\mathcal{V}_{\widetilde{Q}}^*$ is the associated linear space of admissible variations. In (2.14) we impose either homogeneous Dirichlet or homogeneous Neumann boundary conditions, depending on the physical boundary condition types enforced at the first step. More details about the boundary conditions of the viscoelastic problem are given in [14].

3. Coupling algorithm. In this section we briefly recall from [20] the coupling equations and the numerical algorithms for the partitioned solution of a geometrical multiscale problem. Then, we focus on the computation or approximation of the Jacobian entries of the interface problem. For the 3-D FSI model we devise the exact tangent problem, while for the 1-D FSI model we briefly summarize the results of [14]. The methodology presented here is devised for the coupling of the fluid part of the FSI problems. The extension to the solid part is discussed in Section 4.

3.1. Fluid coupling equations. In a geometrical multiscale approach the aim is to couple several heterogeneous models without loosing abstraction and generality. In particular, in Section 2 we introduced two FSI models characterized by different geometrical dimensions and governed by different kind of partial differential equations. The coupling of such different models can be set by imposing the conservation of averaged/integrated quantities over the interfaces, removing any dependency from the geometrical nature and the mathematical formulation of each model [20]. More specifically, for the fluid part of the problem these boundary quantities are the volumetric flow rate $\mathcal{Q}$ and the averaged normal component of the traction vector $\mathcal{S}$, hereafter referred to as the *coupling flow* and the *coupling stress*, respectively. On the j-th coupling interface of the 3-D FSI model these quantities are computed as

$$\mathcal{Q}_j^{\text{3-D}} = \int_{\Gamma^t_{\text{F},j}} \boldsymbol{u}_\text{F} \cdot \boldsymbol{n}_\text{F} \, \mathrm{d}\Gamma, \qquad \mathcal{S}_j^{\text{3-D}} = \frac{1}{\left|\Gamma^t_{\text{F},j}\right|} \int_{\Gamma^t_{\text{F},j}} (\sigma_\text{F} \cdot \boldsymbol{n}_\text{F}) \cdot \boldsymbol{n}_\text{F} \, \mathrm{d}\Gamma,$$

where we assume that each coupling surface $\Gamma^t_{\text{F},j}$, $j = 1, \ldots, n^\Gamma_{\text{FS}}$, is planar.

Remark 1. In the present work we consider the quantity $(\sigma_\text{F} \cdot \boldsymbol{n}_\text{F}) \cdot \boldsymbol{n}_\text{F}$ constant over $\Gamma^t_{\text{F},j}$, $j = 1, \ldots, n^\Gamma_{\text{FS}}$, such that we can rewrite the coupling stress as: $\mathcal{S}_j^{\text{3-D}} = (\sigma_\text{F} \cdot \boldsymbol{n}_\text{F}) \cdot \boldsymbol{n}_\text{F}$. Indeed, as we explain in the next remark, $\mathcal{S}_j^{\text{3-D}}$ has the meaning of the Lagrange multiplier responsible for enforcing the imposition of the flow rate $\mathcal{Q}_j^{\text{3-D}}$ through $\Gamma^t_{\text{F},j}$, $j = 1, \ldots, n^\Gamma_{\text{FS}}$.

Remark 2. Following the approach in [38], the imposition of the coupling flow on a coupling interface of the 3-D FSI fluid problem is addressed in a weak sense through a Lagrange multiplier. This choice leads to a uniform value of the normal component of the traction vector [39] on the same boundary interface. Moreover it is coherent with the other chosen fluid coupling condition, i.e., the coupling stress. Note, however, that the same methodology holds when imposing the coupling flow through a given normal velocity profile.

Remark 3. The 3-D FSI fluid problem needs an additional set of boundary conditions on the two tangential directions lying on $\Gamma^t_{\text{F},j}$, $j = 1, \ldots, n^\Gamma_{\text{FS}}$. Since, for modeling reasons, we assume that at these coupling interfaces the flow is fully developed and orthogonal to the plane, we impose $(\sigma_\text{F} \cdot \boldsymbol{n}_\text{F}) \cdot \boldsymbol{\tau}_{2\text{F}} = 0$ and $(\sigma_\text{F} \cdot \boldsymbol{n}_\text{F}) \cdot \boldsymbol{\tau}_{2\text{F}} = 0$, where $\boldsymbol{\tau}_{1\text{F}}$ and $\boldsymbol{\tau}_{2\text{F}}$ are the two tangential directions.

Regarding the 1-D FSI model we have

$$\text{L}: \begin{cases} \mathcal{Q}_\text{L}^{\text{1-D}} = -Q_\text{L}, \\ \\ \mathcal{S}_\text{L}^{\text{1-D}} = -P_\text{L}, \end{cases} \qquad \text{R}: \begin{cases} \mathcal{Q}_\text{R}^{\text{1-D}} = Q_\text{R}, \\ \\ \mathcal{S}_\text{R}^{\text{1-D}} = -P_\text{R}, \end{cases}$$

where the subscripts L and R stand for left and right sides, respectively.

By using the approach described in [20], we write a set of conservation equations. More precisely, we consider a general network of models connected by $\mathcal{C}$ coupling

nodes: at the c-th coupling node we impose the conservation of mass and the continuity of normal stresses as

$$\begin{cases} \displaystyle\sum_{i=1}^{\mathcal{I}_c} \mathcal{Q}_{c,i} = 0, \\ \mathcal{S}_{c,1} - \mathcal{S}_{c,i} = 0, \quad i = 2, \dots, \mathcal{I}_c, \end{cases} \tag{3.1}$$

where $\mathcal{I}_c$ is the number of interfaces connected by the c-th coupling node, $c = 1, \dots, \mathcal{C}$.

3.2. Numerical approach. For the sake of generality, the interface problem at the c-th coupling node is written in a residual form

$$\boldsymbol{\mathcal{R}}_c = \mathbf{0},$$

where $\boldsymbol{\mathcal{R}}_c$ is the local residuals vector, $c = 1, \dots, \mathcal{C}$. The set of equations (3.1) holds independently from the type of boundary data imposed at each coupling interface, leading to an arbitrary choice of the coupling conditions to be applied on the underlying models. Among the several possible combinations, in [20, Section 2.5] three significant cases are addressed. We briefly recall two of them, the imposition of the coupling stress on all the coupling interfaces

$$\boldsymbol{\mathcal{R}}_c = \begin{pmatrix} \mathcal{Q}_{c,1}\left(\mathcal{S}_c, \cdot\right) + \displaystyle\sum_{i=2}^{\mathcal{I}_c} \mathcal{Q}_{c,i} \\ \mathcal{Q}_{c,2}\left(\mathcal{S}_c, \cdot\right) - \mathcal{Q}_{c,2} \\ \mathcal{Q}_{c,3}\left(\mathcal{S}_c, \cdot\right) - \mathcal{Q}_{c,3} \\ \vdots \\ \mathcal{Q}_{c,\mathcal{I}_c}\left(\mathcal{S}_c, \cdot\right) - \mathcal{Q}_{c,\mathcal{I}_c} \end{pmatrix} \quad \text{for } c \in \mathcal{L}^{\mathcal{S}}, \tag{3.2}$$

and its dual case (coupling flow imposed on all the coupling interfaces)

$$\boldsymbol{\mathcal{R}}_c = \begin{pmatrix} \displaystyle\sum_{i=1}^{\mathcal{I}_c} \mathcal{Q}_{c,i} \\ \mathcal{S}_{c,1}\left(\mathcal{Q}_{c,1}, \cdot\right) - \mathcal{S}_{c,2}\left(\mathcal{Q}_{c,2}, \cdot\right) \\ \mathcal{S}_{c,1}\left(\mathcal{Q}_{c,1}, \cdot\right) - \mathcal{S}_{c,3}\left(\mathcal{Q}_{c,3}, \cdot\right) \\ \vdots \\ \mathcal{S}_{c,1}\left(\mathcal{Q}_{c,1}, \cdot\right) - \mathcal{S}_{c,\mathcal{I}_c}\left(\mathcal{Q}_{c,\mathcal{I}_c}, \cdot\right) \end{pmatrix} \quad \text{for } c \in \mathcal{L}^{\mathcal{Q}}, \tag{3.3}$$

where $\mathcal{L}^{\mathcal{S}}$ and $\mathcal{L}^{\mathcal{Q}}$ denote the set of coupling nodes where coupling stress and coupling flow conditions, respectively, are imposed on the coupling interfaces, while $\mathcal{Q}_{c,i}\left(\mathcal{S}_c, \cdot\right)$ and $\mathcal{S}_{c,i}\left(\mathcal{Q}_{c,i}, \cdot\right)$ are two boundary operators that given a proper set of coupling conditions return the coupling flow and the coupling stress, respectively, at the i-th coupling interface of the c-th coupling node. Note that in (3.2) and (3.3) the operators are global, as they may depend also on non-local coupling quantities, i.e., quantities introduced at other coupling nodes; this dependence is indicated by the dot in the round parentheses. The two strategies result in the following local vectors of unknowns

$$\boldsymbol{\chi}_c = \left(\mathcal{S}_c, \mathcal{Q}_{c,2}, \dots, \mathcal{Q}_{c,\mathcal{I}_c}\right)^{\mathsf{T}} \text{ for } c \in \mathcal{L}^{\mathcal{S}}, \qquad \boldsymbol{\chi}_c = \left(\mathcal{Q}_{c,1}, \mathcal{Q}_{c,2}, \dots, \mathcal{Q}_{c,\mathcal{I}_c}\right)^{\mathsf{T}} \text{ for } c \in \mathcal{L}^{\mathcal{Q}}.$$

Let $\boldsymbol{\chi}_{\mathcal{I}} = \left(\boldsymbol{\chi}_1^{\mathsf{T}}, \boldsymbol{\chi}_2^{\mathsf{T}}, \ldots, \boldsymbol{\chi}_{\mathcal{C}}^{\mathsf{T}}\right)^{\mathsf{T}}$ be the global vector of unknowns of all the coupling interfaces. The solution of the global coupled problem is addressed by using a nonlinear Richardson strategy

$$\boldsymbol{\chi}_{\mathcal{I}}^{k+1} = \boldsymbol{\chi}_{\mathcal{I}}^{k} + \delta\boldsymbol{\chi}_{\mathcal{I}}^{k}, \tag{3.4}$$

until convergence within a suitable tolerance has been achieved. The initial guess $\boldsymbol{\chi}_{\mathcal{I}}^{0}$ is assigned by performing a linear extrapolation of the solution of the previous time steps. Being

$$\boldsymbol{\mathcal{R}}_{\mathcal{I}}\left(\boldsymbol{\chi}\right) = \left(\boldsymbol{\mathcal{R}}_1(\boldsymbol{\chi}_1)^{\mathsf{T}}, \boldsymbol{\mathcal{R}}_2(\boldsymbol{\chi}_2)^{\mathsf{T}}, \ldots, \boldsymbol{\mathcal{R}}_{\mathcal{C}}(\boldsymbol{\chi}_{\mathcal{C}})^{\mathsf{T}}\right)^{\mathsf{T}},$$

the global residuals vector of the interface problem, the update $\delta\boldsymbol{\chi}_{\mathcal{I}}^{k}$ is computed by using either a Newton or an inexact-Newton method

$$\mathcal{J}_{\mathcal{I}}\left(\boldsymbol{\chi}_{\mathcal{I}}^{k}\right)\delta\boldsymbol{\chi}_{\mathcal{I}}^{k} = -\boldsymbol{\mathcal{R}}_{\mathcal{I}}\left(\boldsymbol{\chi}_{\mathcal{I}}^{k}\right),$$

depending on the fact that the Jacobian matrix $\mathcal{J}_{\mathcal{I}}\left(\boldsymbol{\chi}_{\mathcal{I}}\right)$ is either exact or approximated. In both cases, the Jacobian matrix can be filled in two steps. In the first one, the Jacobian graph is built and the required type of entries (coupling flow or coupling stress partial derivatives) are identified. This is done by using the methodology described in [20, Section 3.2.1], which is devised for the most general case. Then, during the second step, the matrix entries can be either computed by solving the tangent problems associated to the coupled models [14, 20], or approximated by using a simpler finite difference approach, which may lead to a good approximation at a reasonable cost [3, 14]. We further discuss this topic in Section 3.3.

Since in presence of 3-D FSI models the assembling of the Jacobian matrix of the interface problem may be too expensive, some further approximations can be introduced. For example, it is possible to reuse the same Jacobian matrix for more than one iteration and eventually more than one time step. However, a better solution in the same direction is to use a Broyden approach for the update of the Jacobian matrix at each nonlinear Richardson iteration. Indeed, this approach has been proven to perform successfully for cardiovascular applications made of networks of 1-D models [3, 14] and for heterogeneous networks of rigid fluid problems [40], requiring just a cheap evaluation of the global residuals vector of the interface problem.

3.3. Jacobian entries computation. By definition, the exact Jacobian matrix of the global interface problem is given by the derivative of the residuals vector with respect to the coupling unknowns, i.e.,

$$\mathcal{J}_{\mathcal{I}}\left(\boldsymbol{\chi}_{\mathcal{I}}\right) = \frac{\partial\boldsymbol{\mathcal{R}}_{\mathcal{I}}\left(\boldsymbol{\chi}_{\mathcal{I}}\right)}{\partial\boldsymbol{\chi}_{\mathcal{I}}}.$$

The residuals and the unknowns vectors depend from the type of coupling conditions imposed at each node of the network. Therefore, the block structure of the Jacobian and the type of matrix entries are problem dependent. From (3.2) and (3.3) we observe that, beside the constant entries in general there are no more than four possible coefficient types, corresponding to the partial derivatives of the two boundary operators with respect to the coupling flow and to the coupling stress, i.e.,

$$\begin{aligned}
&\frac{\partial\mathcal{Q}_{c,i}\left(\mathcal{S}_c,\cdot\right)}{\partial\mathcal{Q}} \quad \text{and} \quad \frac{\partial\mathcal{Q}_{c,i}\left(\mathcal{S}_c,\cdot\right)}{\partial\mathcal{S}}, \quad i = 1,\ldots,\mathcal{I}_c, \quad \text{for } c \in \mathcal{L}^{\mathcal{Q}}.\\
&\frac{\partial\mathcal{S}_{c,i}\left(\mathcal{Q}_{c,i},\cdot\right)}{\partial\mathcal{Q}} \quad \text{and} \quad \frac{\partial\mathcal{S}_{c,i}\left(\mathcal{Q}_{c,i},\cdot\right)}{\partial\mathcal{S}}, \quad i = 1,\ldots,\mathcal{I}_c, \quad \text{for } c \in \mathcal{L}^{\mathcal{Q}}.
\end{aligned} \tag{3.5}$$

In the following, for both FSI models described in Section 2 we provide a suitable numerical approach for the computation or approximation of these Jacobian entries.

3.3.1. 3-D FSI Jacobian entries. In Section 2.1.3 we described a Newton method for the solution of the 3-D FSI problem with the exact computation of the FSI Jacobian matrix $\mathcal{J}_{\text{FSI}}$ in both the GCE and FI approaches. No matter which time discretization scheme is used, the Jacobian matrix of the FSI problem serves also for the computation of the Jacobian entries of the interface problems. For each coupling interface $\Gamma^t_{\text{F},j}$, $j = 1, \dots, n^{\Gamma}_{\text{FS}}$, the tangent problem associated to the 3-D FSI model reads:

$$\mathcal{J}_{\text{FSI}}\left(\boldsymbol{u}^k_{\text{FSI}}\right)\delta\boldsymbol{u}_{\text{FSI},\Gamma^t_{\text{F},j}} = \boldsymbol{b}_{\text{FSI},\Gamma^t_{\text{F},j}},$$

where $\boldsymbol{u}^k_{\text{FSI}}$ is the solution of the FSI problem obtained during the computation of the residuals vector of the k-th nonlinear Richardson iteration of the interface problem. The entries of $\boldsymbol{b}_{\text{FSI},\Gamma^t_{\text{F},j}}$ are null apart from the contribution given by the unitary coupling condition applied in $\Gamma^t_{\text{F},j}$, and $\delta\boldsymbol{u}_{\text{FSI},\Gamma^t_{\text{F},j}}$ is the variation of the global FSI solution vector due to a unitary perturbation of the coupling condition in $\Gamma^t_{\text{F},j}$. Note that this is equivalent to solve problem (2.8) with a different right-hand side which takes into account the local network topology.

Remark 4. From the computational viewpoint, it is necessary to solve one tangent problem for each coupling interface of the 3-D FSI model. However, the Jacobian matrix is the same for all the cases. Moreover, it is already available from the previous Newton iterations of the FSI problem (see equation (2.7)).

Remark 5. In the GCE time discretization approach, problem (2.9) is solved just once per time step, at the first nonlinear Richardson iteration of the interface problem. Indeed, it does not depend on any fluid coupling quantity.

The values of the Jacobian entries are then retrieved from the solution of the FSI tangent problem. More precisely, given $\delta\boldsymbol{u}_{\text{FSI},\Gamma^t_{\text{F},j}}$, the partial derivatives of the boundary operators with respect to the coupling condition in $\Gamma^t_{\text{F},j}$, are obtained by computing the coupling flow and the coupling stress values on the j-th coupling interface.

3.3.2. 1-D FSI Jacobian entries. In Section 2.2.2 we briefly discussed about the limitation imposed on the time step by the CFL condition. This limitation is particularly severe when coupling the 1-D FSI model with computationally expensive 3-D models, e.g., the 3-D FSI model described in Section 2.1. In fact, to perform the nonlinear Richardson iterations on the global coupled problem, all the elements in the network must use the same time step, thus the element that requires the smallest time step forces the entire system to advance the computations at its own time step. This goes in the opposite direction with respect to the need for a large time step for the coupled 3-D FSI problem, in order to minimize the computational cost. For instance, when solving the blood flow in an arterial network, the time step required for the solution of the 1-D FSI segments in the circle of Willis may be around two orders of magnitude smaller than the one needed by a 3-D FSI vessel embedded in the arterial tree.

This problem is addressed in [14] by introducing a two-level time step technique. More precisely, the inner time step meets the local 1-D CFL requirements, being different for each 1-D FSI model, while the outer time step is used for the global coupling between the models, i.e., (3.1) is satisfied just at this outer level. At the

inner time level, the boundary conditions for the 1-D problems are provided by using a Lagrange polynomial interpolation of the coupling conditions. This approach allows us to choose the outer global time step according to the requirement of any 3-D FSI problem in the network.

The computation of the Jacobian coefficients of the 1-D FSI problem can be addressed by solving the associated exact tangent problem, as described in [14]. However, in presence of inner time steps, the recursion of the problem creates an obstacle that prevents to reach an analytical expression of these entries. A possible alternative is to devise an approximated version of the tangent problem. Nevertheless, as shown in [14], a finite difference approach is more effective in this case. By following this latter approach, the derivative of the coupling stress on the left side of the 1-D model with respect to the coupling flow on the same side is given by

$$\frac{\partial \mathcal{S}_{\mathrm{L}}^{n+1}}{\partial \mathcal{Q}_{\mathrm{L}}} \cong \frac{\mathcal{S}_{\mathrm{L}}\left(\mathcal{Q}_{\mathrm{L}}^{n+1}+\delta\mathcal{Q}_{\mathrm{L}},\cdot\right)-\mathcal{S}_{\mathrm{L}}\left(\mathcal{Q}_{\mathrm{L}}^{n+1},\cdot\right)}{\delta\mathcal{Q}_{\mathrm{L}}},$$

where $\delta\mathcal{Q}_{\mathrm{L}}$ is a properly chosen volumetric flow rate perturbation parameter and the dot represents the non-local coupling condition, i.e., the coupling condition on the right side of the 1-D segment. The other entry types are addressed similarly. For more details see [14].

4. Interface conditions for the 3-D solid problem. As discussed in Section 2.1, problem (2.4) requires n_{FS}^{Γ} boundary conditions on the inlet and outlet solid rings $\Gamma_{\mathrm{S},j}^{0}$, $j=1,\ldots,n_{\mathrm{FS}}^{\Gamma}$. These boundary conditions can be either given data, or computed by using information related to the surrounding models. In this section, we propose three different approaches to close the solid problem. For each approach we highlight the main pros and cons. The analysis of the numerically-induced wave reflections in a geometrical multiscale setting is deferred until Section 5.

4.1. Clamped solid ring boundary condition. A first approach, widely used in the literature, consists in clamping the solid rings of the 3-D FSI model by imposing a homogeneous Dirichlet boundary condition on the solid displacement, i.e.,

$$\boldsymbol{d}_{\mathrm{S}}=\mathbf{0} \qquad \text{on } \Gamma_{\mathrm{S},j}^{0}\times(0,T], \tag{4.1}$$

with $j=1,\ldots,n_{\mathrm{FS}}^{\Gamma}$. The main advantage of this approach is the very easy implementation, since no additional equations are required. However, this type of boundary condition is far from representing the behavior of the arterial wall at those locations. First of all, the value of the solid displacement near the clamped rings cannot be considered reliable, neither are the values of other physical quantities such as the wall stress state. In addition, spurious backward reflections may be generated at the outlets of the 3-D domain; in a geometrical multiscale setting, this problem can also affect the surrounding 1-D FSI models.

4.2. Free solid ring boundary condition. In order to represent a more realistic behavior of the arterial wall at the inlet/outlet rings, a possible solution would be to impose homogeneous Neumann boundary conditions on the normal component of the first Piola–Kirchhoff stress tensor, i.e.,

$$\sigma_{\mathrm{S}}\cdot\boldsymbol{n}_{\mathrm{S}}=\mathbf{0} \qquad \text{on } \Gamma_{\mathrm{S},j}^{0}\times(0,T], \tag{4.2}$$

with $j=1,\ldots,n_{\mathrm{FS}}^{\Gamma}$. However, this approach may lead to an ill-posed problem, since the six rigid-body modes of the vessel are not constrained. In addition, from the

physical viewpoint, the continuation of the vessel beyond the boundaries is not represented; in particular, the solid rings are free to move along the longitudinal direction. To address these issues, we devise a different approach, i.e.,

$$\begin{cases} \boldsymbol{d}_{\mathrm{S}} \cdot \boldsymbol{n}_{\mathrm{S}} = 0 & \text{on } \Gamma^0_{\mathrm{S},j} \times (0,T], \\ \displaystyle\int_{\Gamma^0_{\mathrm{S},j}} \boldsymbol{d}_{\mathrm{S}} \cdot \boldsymbol{\tau}_{1\mathrm{S}} \,\mathrm{d}\Gamma = 0, \quad \int_{\Gamma^0_{\mathrm{S},j}} \boldsymbol{d}_{\mathrm{S}} \cdot \boldsymbol{\tau}_{2\mathrm{S}} \,\mathrm{d}\Gamma = 0 & \text{on } \Gamma^0_{\mathrm{S},j} \times (0,T], \\ \displaystyle\int_{\Gamma^0_{\mathrm{S},j}} \left(\boldsymbol{\nabla}_\Gamma \wedge [0, \quad \boldsymbol{d}_{\mathrm{S}} \cdot \boldsymbol{\tau}_{1\mathrm{S}}, \quad \boldsymbol{d}_{\mathrm{S}} \cdot \boldsymbol{\tau}_{2\mathrm{S}}]^{\mathsf{T}} \right) \cdot \boldsymbol{n}_{\mathrm{S}} \,\mathrm{d}\Gamma = 0 & \text{on } \Gamma^0_{\mathrm{S},j} \times (0,T], \end{cases} \tag{4.3}$$

where $\boldsymbol{\tau}_{1\mathrm{S}}$ and $\boldsymbol{\tau}_{2\mathrm{S}}$ are the two tangential directions lying on $\Gamma^0_{\mathrm{S},j}$, $j = 1, \ldots, n^{\Gamma}_{\mathrm{FS}}$. The first restriction prevents the normal displacement of the solid ring (in the longitudinal direction), representing the continuation of the vessel beyond the domain boundaries. In addition, it removes three rigid-body modes: the normal translation and the two non-planar rotations. The second restriction removes the two planar translation rigid-body modes, without imposing any constraint on the area of the vessel. More precisely, the boundary rings can enlarge or reduce their size around a fixed geometric center. This restriction can be rewritten in the following form:

$$\int_{\Gamma^0_{\mathrm{S},j}} \mathrm{P}\boldsymbol{d}_{\mathrm{S}} \,\mathrm{d}\Gamma = \boldsymbol{0} \qquad \text{on } \Gamma^0_{\mathrm{S},j} \times (0,T],$$

being $\mathrm{P} = \mathrm{I} - \boldsymbol{n}_{\mathrm{S}} \cdot \boldsymbol{n}_{\mathrm{S}}^{\mathsf{T}}$ the local projection operator over the tangential plane where each solid ring lies. Finally, the third restriction removes the planar rotation rigid-body mode. With the same approach as before, it can be rewritten as follows:

$$\int_{\Gamma^0_{\mathrm{S},j}} (\boldsymbol{\nabla}_\Gamma \wedge \mathrm{P}\boldsymbol{d}_{\mathrm{S}}) \cdot \boldsymbol{n}_{\mathrm{S}} \,\mathrm{d}\Gamma = 0 \qquad \text{on } \Gamma^0_{\mathrm{S},j} \times (0,T].$$

Note that $\mathrm{P}\boldsymbol{d}_{\mathrm{S}}$ is a vector lying over the two-dimensional plane defined by its normal $\boldsymbol{n}_{\mathrm{S}}$, while $\boldsymbol{\nabla}_\Gamma \wedge$ denotes the curl operator defined in terms of the tangential coordinates and applied to such a tangent vector, which gives a vector aligned with the normal vector $\boldsymbol{n}_{\mathrm{S}}$. Furthermore, we can use a variant of the Green theorem to change the last restriction into the following one

$$\int_{C^0_{\mathrm{S},j}} \mathrm{P}\boldsymbol{d}_{\mathrm{S}} \cdot \boldsymbol{\tau}_C \,\mathrm{d}C = 0 \qquad \text{on } C^0_{\mathrm{S},j} \times (0,T],$$

where $C^0_{\mathrm{S},j}$ denotes the internal and external curves that define the ring $\Gamma^0_{\mathrm{S},j}$, $j = 1, \ldots, n^{\Gamma}_{\mathrm{FS}}$, and $\boldsymbol{\tau}_C$ is the tangent vector to these curves.

Remark 6. In the most general case, where there exists at least one solid ring whose normal is not aligned with one of the Cartesian axes, it is convenient to impose the three restrictions by introducing different Lagrange multipliers in the weak form of the solid problem.

Remark 7. If there exists at least three boundary solid rings equipped with a different normal, all the six rigid-body modes can be removed by imposing just the first restriction. However, from the physical point of view, the other two restrictions are still relevant.

The main advantage of this approach with respect to (4.1), is the very general way of addressing the boundary conditions for the 3-D solid problem, without over-constraining the structure displacement at the coupling interfaces. In particular,

it suits both stand-alone 3-D FSI problems, and geometrical multiscale approaches, where the 3-D domain is coupled with 1-D problems although, in the later one, the continuity of the area is not guaranteed.

4.3. Scaled area solid ring boundary condition. A third different strategy is to prescribe the value of the boundary area of each fluid coupling interface. Following the approach devised in [21], this can be done by prescribing a radial displacement of the internal contour of the j-th 3-D solid ring, $j = 1, \dots, n_{\mathrm{FS}}^{\Gamma}$, i.e.,

$$\begin{cases} \boldsymbol{d}_{\mathrm{S}} \cdot \boldsymbol{n}_{\mathrm{S}} = 0 & \text{on } \Gamma_{\mathrm{I}}^0 \cap \Gamma_{\mathrm{S},j}^0 \times (0,T], \\ \left[\boldsymbol{d}_{\mathrm{S}} - \Psi_j^t \left(\boldsymbol{x}^0 - \boldsymbol{x}_{\mathrm{G},j}^0\right)\right] \cdot \boldsymbol{\tau}_{1\mathrm{S}} = 0 & \text{on } \Gamma_{\mathrm{I}}^0 \cap \Gamma_{\mathrm{S},j}^0 \times (0,T], \\ \left[\boldsymbol{d}_{\mathrm{S}} - \Psi_j^t \left(\boldsymbol{x}^0 - \boldsymbol{x}_{\mathrm{G},j}^0\right)\right] \cdot \boldsymbol{\tau}_{2\mathrm{S}} = 0 & \text{on } \Gamma_{\mathrm{I}}^0 \cap \Gamma_{\mathrm{S},j}^0 \times (0,T], \end{cases} \tag{4.4}$$

which corresponds to a geometric rescaling of the area, where the scale factor is defined as

$$\Psi_j^t = \sqrt{\frac{A_j^t}{A_j^0}} - 1,$$

being A_j^0 and $\boldsymbol{x}_{\mathrm{G},j}^0$ the reference area of the j-th coupling interface of the 3-D fluid problem and its geometric center, respectively. This approach preserves the original shape of each 3-D solid ring, whose size is scaled by the value of the given boundary area A_j^t.

Remark 8. As (4.3) does, also (4.4) constrains all the rigid-body modes of the 3-D FSI problem. However, this condition is applied only to the inner contour of the boundary rings, i.e., $\Gamma_{\mathrm{I}}^0 \cap \Gamma_{\mathrm{S},j}^0$, $j = 1, \dots, n_{\mathrm{FS}}^{\Gamma}$. To close the 3-D FSI solid problem, we need to impose an additional boundary condition on $\Gamma_{\mathrm{S},j}^0 \backslash \Gamma_{\mathrm{I}}^0 \cap \Gamma_{\mathrm{S},j}^0 \times (0,T]$, $j = 1, \dots, n_{\mathrm{FS}}^{\Gamma}$, which can be either (4.2) or (4.3). The former leaves some degrees of freedom to the displacement of the boundary solid rings, e.g., the external contour of the rings can move in the longitudinal direction or rotate on itself. However if the thickness of the solid wall is small with respect to the vessel area, these movements are negligible.

Since, in general, boundary data of the vessels area are not available for cardiovascular simulations, the value of the area can be obtained either by modeling its dynamic through a local simple model, or, in a geometrical multiscale setting, by imposing the continuity of the boundary area with the surrounding models. The latter case is explored in the next section. Regarding the former one, the dynamic of the local boundary area can be expressed as a function of the time and of some local boundary quantities, e.g., volumetric flow rate and average pressure. Among the several possibilities, a straightforward choice is to use the inverse of the 1-D pressure-area relation described in (2.11), eventually adding some further contributions, such as the inertia of the wall, in order to match the physics of the 3-D solid problem given in (2.4).

4.3.1. Continuity of the vessel area. In a geometrical multiscale setting, the interfaces of the 3-D FSI model are generally connected with the ones of reduced models, such as the 1-D FSI model. In this case, it is possible to write an additional relation at the coupling interfaces of the two heterogeneous FSI models to impose the continuity of the area of the connected vessels. To do this, let us first introduce a new averaged quantity on each boundary interface, i.e, the area of the fluid section $\mathcal{A}$,

hereafter referred to as the *coupling area*. On the j-th coupling interface of the 3-D FSI this quantity is computed as

$$\mathcal{A}_j^{\text{3-D}} = \left|\Gamma_{\text{F},j}^t\right|,$$

with $j = 1, \dots, n_{\text{FS}}^{\Gamma}$. Regarding the 1-D FSI model it is given by

$$\text{L}: \ \mathcal{A}_{\text{L}}^{\text{1-D}} = A_{\text{L}}, \qquad \text{R}: \ \mathcal{A}_{\text{R}}^{\text{1-D}} = A_{\text{R}}.$$

Let $\mathcal{L}^{\mathcal{A}}$ be the set of coupling nodes where the continuity of the area between the two heterogeneous FSI models is imposed. There, (3.1) becomes

$$\begin{cases} \mathcal{Q}_{c,1}^{\text{1-D}} + \mathcal{Q}_{c,2}^{\text{3-D}} = 0, \\ \mathcal{S}_{c,1}^{\text{1-D}} - \mathcal{S}_{c,2}^{\text{3-D}} = 0, \\ \mathcal{A}_{c,1}^{\text{1-D}} - \mathcal{A}_{c,2}^{\text{3-D}} = 0, \end{cases} \tag{4.5}$$

where $c \in \mathcal{L}^{\mathcal{A}}$ and, for the sake of clarity, the model to which each quantity belongs is indicated in the superscript. We remark that (4.5) is written for the specific case of a 3-D FSI interface coupled with a single 1-D FSI model. In the case of a generalization to two or more 1-D models connected to the same 3-D FSI interface setting the continuity of the area does not make sense, and for this reason we do not address this case.

As described in Section 2.2, the 1-D FSI problem needs just one physical boundary condition on each side of the segment; by imposing either the coupling flow or the coupling stress, the value of the coupling area of the 1-D segment is already determined by the solution of the 1-D problem. From the numerical viewpoint, this creates the opportunity of using three different time discretizations schemes to solve the problem at the coupling interfaces.

Explicit. The area of each interface of the 3-D FSI model at time t^{n+1} is imposed equal to the one of the nearby 1-D interface at the previous time step. By using this approach, each scale factor Ψ_j^t, $j = 1, \dots, n_{\text{FS}}^{\Gamma}$, is computed explicitly at the beginning of each time step. Therefore, the residual form at the coupling interfaces is still written just in terms of the coupling flow and the coupling stress, as in (3.2) and (3.3). The flow diagram of this scheme is shown in Figure 4.1.

Implicit with hierarchy. The area of each interface of the 3-D FSI model at time t^{n+1} is imposed equal to the one of the nearby 1-D interface at the same time step. This is done by introducing a hierarchy among the models, such that at each nonlinear Richardson iteration first we solve the 1-D FSI models, computing the boundary area of each 1-D segment, and then we use these values to close and solve the nearby 3-D FSI models. As in the explicit case, the residual form at the coupling interfaces is written in terms of the coupling flow and the coupling stress. However, the scale factor Ψ_j^t, $j = 1, \dots, n_{\text{FS}}^{\Gamma}$, is updated with the new value of the area of the 1-D problem at each nonlinear Richardson iteration of the interface problem. Since the dependence on the varying area is not taken into account in the 3-D boundary operators of (3.2) and (3.3), the resulting Jacobian matrix is inexact and might lead to an increase of the number of iterations. The flow diagram of this scheme is shown in Figure 4.2.

Implicit without hierarchy. As in the previous case, the area of each interface of the 3-D FSI model at time t^{n+1} is imposed equal to the one of the nearby 1-D

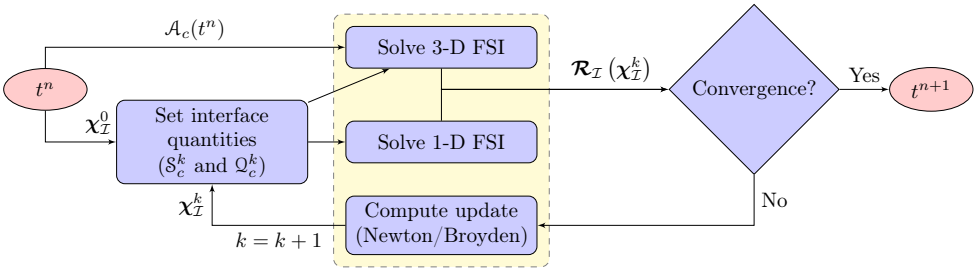

Figure 4.1: Algorithm flow diagram, for the coupling of two geometrically-heterogeneous FSI models, by using the explicit time discretization scheme for the continuity of the vessel area. In the diagram $\boldsymbol{\chi}_{\mathcal{I}}$ includes only fluid quantities, i.e., $\boldsymbol{\chi}_c = (\mathcal{S}_c, \mathcal{Q}_{c,2})^{\mathsf{T}}$ for $c \in \mathcal{L}^{\mathcal{S}}$ and $\boldsymbol{\chi}_c = (\mathcal{Q}_{c,1}, \mathcal{Q}_{c,2})^{\mathsf{T}}$ for $c \in \mathcal{L}^{\mathcal{Q}}$.

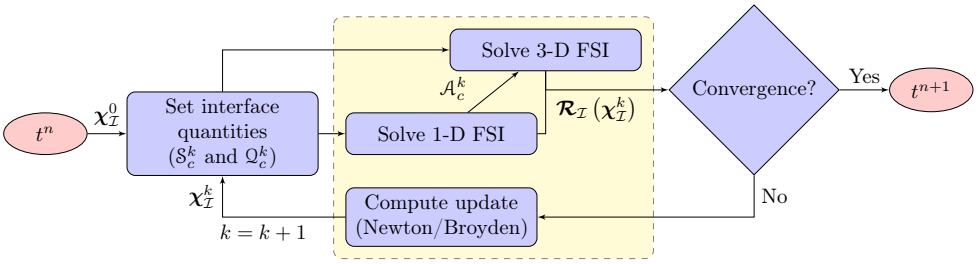

Figure 4.2: Algorithm flow diagram for the coupling of two geometrically-heterogeneous FSI models, by using the implicit with hierarchy time discretization scheme for the continuity of the vessel area. In the diagram $\boldsymbol{\chi}_{\mathcal{I}}$ includes only fluid quantities, i.e., $\boldsymbol{\chi}_c = (\mathcal{S}_c, \mathcal{Q}_{c,2})^{\mathsf{T}}$ for $c \in \mathcal{L}^{\mathcal{S}}$ and $\boldsymbol{\chi}_c = (\mathcal{Q}_{c,1}, \mathcal{Q}_{c,2})^{\mathsf{T}}$ for $c \in \mathcal{L}^{\mathcal{Q}}$.

interface at the same time step. However, instead of introducing a hierarchy among the models, we impose the continuity of the area in the residual formulation, such that (3.2) becomes

$$\boldsymbol{\mathcal{R}}_c = \begin{pmatrix} \mathcal{Q}_{c,1}^{1\text{-D}}(\mathcal{S}_c, \cdot) + \mathcal{Q}_c \\ \mathcal{Q}_{c,2}^{3\text{-D}}(\mathcal{S}_c, \mathcal{A}_c, \cdot) - \mathcal{Q}_c \\ \mathcal{A}_{c,1}^{1\text{-D}}(\mathcal{S}_c, \cdot) - \mathcal{A}_c \end{pmatrix} \quad \text{for } c \in \mathcal{L}^{\mathcal{AS}}, \tag{4.6}$$

and (3.3) becomes

$$\boldsymbol{\mathcal{R}}_c = \begin{pmatrix} \mathcal{Q}_{c,1} + \mathcal{Q}_{c,2} \\ \mathcal{S}_{c,1}^{1\text{-D}}(\mathcal{Q}_{c,1}, \cdot) - \mathcal{S}_{c,2}^{3\text{-D}}(\mathcal{Q}_{c,2}, \mathcal{A}_c, \cdot) \\ \mathcal{A}_{c,1}^{1\text{-D}}(\mathcal{Q}_{c,1}, \cdot) - \mathcal{A}_c \end{pmatrix} \quad \text{for } c \in \mathcal{L}^{\mathcal{AQ}}, \tag{4.7}$$

where $\mathcal{L}^{\mathcal{AS}}$ and $\mathcal{L}^{\mathcal{AQ}}$ are the counterparts of $\mathcal{L}^{\mathcal{S}}$ and $\mathcal{L}^{\mathcal{Q}}$, with $\mathcal{L}^{\mathcal{A}} = \mathcal{L}^{\mathcal{AS}} \cup \mathcal{L}^{\mathcal{AQ}}$, and $\mathcal{A}_{c,i}(\cdot, \cdot)$ is a boundary operator that given a proper set of coupling conditions returns the coupling area at the i-th coupling interface of the c-th coupling node.

Remark 9. In the development discussed in Section 3 the conservation equations do not imply any specific choice of the coupling conditions, leaving the flexibility to impose either the coupling flow or the coupling stress on each coupling interface. On

the contrary, the set of equations (4.5) requires a particular care due to the presence of the coupling area. More precisely, the coupling area can be imposed only on the 3-D FSI problem, since the 1-D FSI model needs just one physical boundary condition on each side of the segment. Therefore, the third equation in (4.6) and (4.7) cannot be replaced with an equivalent version written by replacing the 1-D boundary area operator with the 3-D one. For instance, in terms of components, in (4.6) notice that, at the c-th interface, the 3-D model receives as input $(\mathcal{S}_c, \mathcal{A}_c)$ and yield as output $\mathcal{Q}_{c,2}^{\text{3-D}}$, while the 1-D model receives $\mathcal{S}_c$ and gives back $(\mathcal{Q}_{c,1}^{\text{1-D}}, \mathcal{A}_{c,1}^{\text{1-D}})$.

The two implicit coupling strategies result in the following local vectors of unknowns

$$\boldsymbol{\chi}_c = (\mathcal{S}_c, \mathcal{Q}_c, \mathcal{A}_c)^{\mathsf{T}} \text{ for } c \in \mathcal{L}^{\mathcal{AS}}, \qquad \boldsymbol{\chi}_c = (\mathcal{Q}_{c,1}, \mathcal{Q}_{c,2}, \mathcal{A}_c)^{\mathsf{T}} \text{ for } c \in \mathcal{L}^{\mathcal{AQ}},$$

such that the solution of the global coupled problem can be again addressed by using a nonlinear Richardson approach, as in (3.4). With respect to the development presented in Section 3.3, the only difference consists in the dependence of the residual from the coupling area, such that four new Jacobian entry types need to be computed/approximated to fill the Jacobian matrix in the most general case:

- $\dfrac{\partial \mathcal{Q}_{c,i}(\mathcal{S}_c, \mathcal{A}_c, \cdot)}{\partial \mathcal{A}}$ and $\dfrac{\partial \mathcal{S}_{c,i}(\mathcal{Q}_{c,i}, \mathcal{A}_c, \cdot)}{\partial \mathcal{A}}$ belong just to the 3-D FSI model and can be computed by solving the associated tangent problem;
- $\dfrac{\partial \mathcal{A}_{c,i}(\mathcal{S}_c, \cdot)}{\partial \mathcal{S}}$ and $\dfrac{\partial \mathcal{A}_{c,i}(\mathcal{Q}_{c,i}, \cdot)}{\partial \mathcal{Q}}$ belong just to the 1-D FSI model and can be approximated by using a finite difference technique.

The flow diagram of this scheme is shown in Figure 4.3. One of the main advantages of this approach with respect to the previous one, is that no hierarchy must be established among the models, such that, in a parallel framework, each model can be solved at the same time on different machines. In addition, the Jacobian matrix of the interface problem is still exact a part from other approximations introduced at the numerical level, i.e., the finite difference approximation of the 1-D FSI entries.

Remark 10. If convergence is achieved, both the *implicit with hierarchy* and the *implicit without hierarchy* approaches yield the same solution.

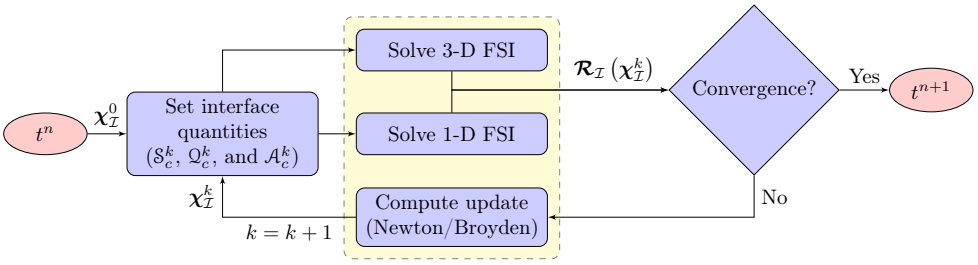

Figure 4.3: Algorithm flow diagram for the coupling of two geometrically-heterogeneous FSI models, by using the implicit without hierarchy time discretization scheme for the continuity of the vessel area. In the diagram, $\boldsymbol{\chi}_{\mathcal{I}}$ includes both the fluid quantities and the vessel area, i.e., $\boldsymbol{\chi}_c = (\mathcal{S}_c, \mathcal{Q}_{c,2}, \mathcal{A}_c)^{\mathsf{T}}$ for $c \in \mathcal{L}^{\mathcal{AS}}$ and $\boldsymbol{\chi}_c = (\mathcal{Q}_{c,1}, \mathcal{Q}_{c,2}, \mathcal{A}_c)^{\mathsf{T}}$ for $c \in \mathcal{L}^{\mathcal{AQ}}$.

4.4. Qualitative comparison of the solid boundary conditions. Finally, it is worthwhile to summarize the main pros and cons of the three methodologies

described above. This comparison is shown in Table 4.1. For the case of a geometrical multiscale problem, a quantitative analysis of the wave reflections at the coupling interfaces is addressed in Section 5.

Table 4.1: Qualitative comparison of the main pros and cons of each proposed interface ring boundary condition for the 3-D solid problem. Note that in the third column some comments depend on the chosen approach (local model vs. continuity of the vessel area).

	Clamped	Free	Scaled area
Code implementation	Very easy	Complex	Complex
Physics at the boundaries	Unrealistic	Realistic	Realistic
Continuity of the vessel area	No	No	No/Yes
Usable in stand-alone 3-D FSI problems	Yes	Yes	Yes/No
Usable in geometrical multiscale problems	Yes	Yes	Yes

5. Wave reflection analysis in a series of pipes. In this section, we make use of simple benchmark examples to compare the behavior of the three proposed interface conditions introduced in Section 4 for the closure of the 3-D solid problem. In particular, we focus our analysis on the spurious backward wave reflections that might be generated at the coupling interfaces between two dimensionally-heterogeneous pipes. In order to have a full overview of the phenomena we analyze both the case of a 1-D wave flow that enters in a 3-D pipe, and the inverse one, i.e., a 3-D wave flow that enters in a 1-D pipe. In both cases, on the leftmost side we impose a single flow rate wave defined as

$$Q(t) = \begin{cases} -\sin\left(\dfrac{2\pi t}{T_{\mathrm{w}}}\right)^2 & t < \dfrac{T_{\mathrm{w}}}{2}, \\ 0 & \text{otherwise}, \end{cases}$$

where $T_{\mathrm{w}} = 0.005$ is the chosen wave period. On the rightmost side, a proper absorbing boundary condition is applied [1, 5]. The interface problem is defined by imposing the coupling stress on the coupling interfaces. In the following, unless otherwise specified, the reference dimensionless parameters that define the problem are: $\rho_{\mathrm{F}} = 1$, $\mu_{\mathrm{F}} = 0.035$, $\alpha_{\mathrm{F}} = 1.1$, $A^0 = \pi$, $h_{\mathrm{S}} = 0.1$, $E_{\mathrm{S}} = 3000000$, $\rho_{\mathrm{S}} = 0$, and $\gamma_{\mathrm{S}} = 0$. Note that with this choice of ρ_{S} and γ_{S}, the inertia and the viscoelastic effects of the wall are neglected in both the FSI models. The Poisson ratio ν_{S} is 0.5 for the 1-D FSI model and 0.475 for the 3-D FSI model. The length L of each pipe is equal to 3. On the solid external wall $\Gamma^0_{\mathrm{S,ext}}$ of the 3-D FSI problem we apply an homogeneous Neumann boundary condition, while we set $P_{\mathrm{ext}} = 0$ in the 1-D FSI problem.

The imposed tolerance for the interface problem is 10^{-6}, while the one for the 3-D FSI problem is 10^{-7}. The mesh of the fluid part of the 3-D pipe consists of 137712 tetrahedral elements with 25077 vertices, while the solid part is made of 51984 tetrahedral elements with 11856 vertices. The corresponding average space discretization for the fluid and solid problems are 0.094 and 0.092, respectively. Regarding the 1-D FSI pipe, we use a uniform space discretization of 0.1, corresponding to 31 vertices. The global time step is set equal to 10^{-5}; since this is quite a small value, we use the GCE time discretization scheme, introduced in Section 2.1.3, to

solve the 3-D FSI problem. All the simulations last 1500 time steps ($T = 0.0015$), which is the time needed by the flow wave to reach the rightmost side of the problems.

5.1. From 1-D to 3-D wave flow propagation. The first case we analyze is described in Figure 5.1. More precisely, we study the reflection amplitude generated at the coupling interfaces when a wave propagates from a 1-D FSI segment (on the left) to a 3-D FSI pipe (on the right), see Figure 5.1(a). We consider as a reference case the solution computed by solving the problem in Figure 5.1(b), i.e., a single 1-D segment of length 6.

(a) (b)

Figure 5.1: Schematic representation of the benchmark case. (a) The wave flow propagates from the 1-D FSI model to the 3-D FSI one. The length of each pipe is equal to 3. (b) The reference case: a single 1-D FSI pipe of length 6.

The results are summarized in Figure 5.2. In particular, on the x-axis we plot the normalized time, while on the y-axis we plot the difference between the volumetric flow rate in the heterogeneous case (see Figure 5.1(a)) and the one given by the reference case (see Figure 5.1(b)), namely ΔQ, normalized over the maximum amplitude of the inflow wave. This quantity coincides with the normalized reflection wave generated at the coupling interface. Note that a similar analysis can be done in terms of pressure waves, leading to the same conclusions.

First of all we can observe that, as expected, the amplitude of the reflection is always larger when the 3-D solid ring is clamped. More precisely, the reflection generated by using such a constraining boundary condition is around twice the size of the one observed when the other two approaches are employed, motivating the need of such more relaxed conditions on the coupling interface. On the contrary, there is no clear advantage in prescribing the continuity of the area of the pipes, with respect to let the deformation of the 3-D boundary solid ring free. Indeed, such behavior depends upon the specific case (see Figures 5.2(b) and 5.2(c) for varying Young modulus).

Regarding the sensitivity analysis with respect to the main 3-D solid parameters, we observe that the value of the Young modulus has an impact on the reflection, even if the shape of the wave does not change significantly. More precisely, the vertical difference between the subsequent peaks in the wave is almost constant such that the amplitude of the reflection is almost the same. On the contrary, the Poisson ratio does not have any effect on the reflection. Finally, we observe that modeling the inertia of the 3-D solid wall leads to significant differences only in presence of the free solid ring boundary condition. This is motivated by the fact that, in the other two cases, the size of the area is controlled by the boundary condition, such that the boundary inertial effects are smooth out.

Last but not least, in Figure 5.3 we study the reflection amplitude as a function of the 3-D mesh size. The results show an opposite behavior between the approach

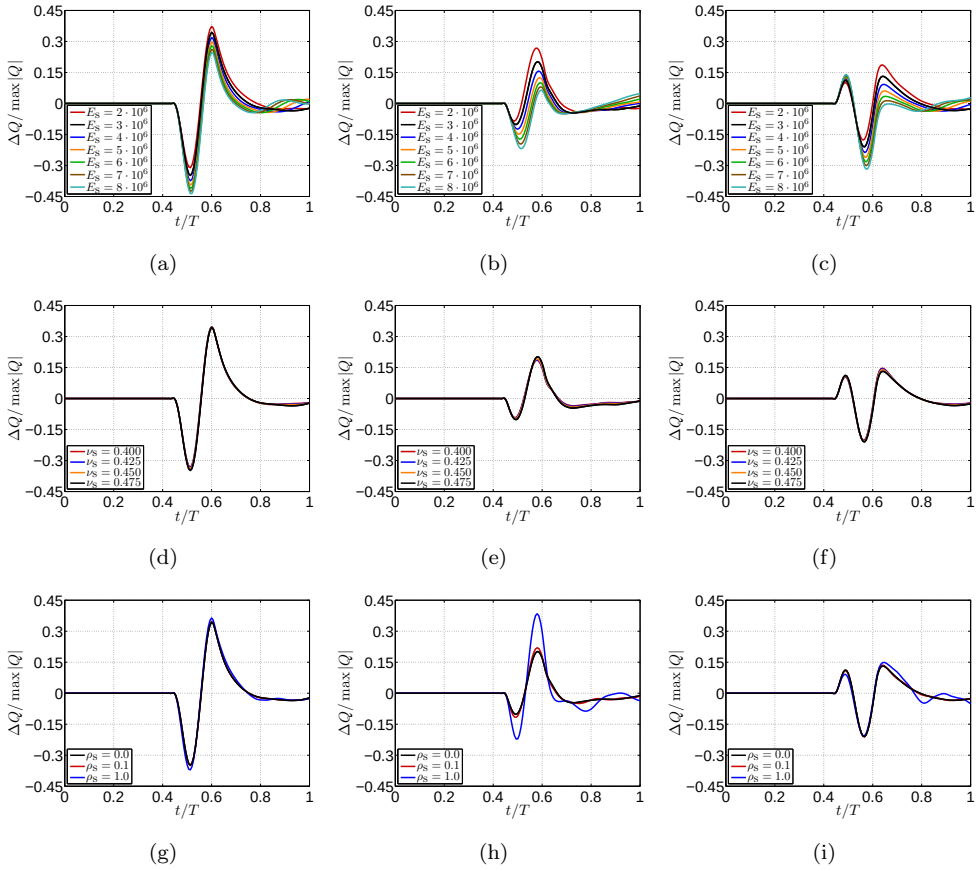

Figure 5.2: Volumetric flow rate wave reflection at the coupling interfaces for different values of the main 3-D solid parameters. In all the figures, the black curve corresponds to the reference parameters. (a,b,c) Varying Young modulus. (d,e,f) Varying Poisson ratio. (g,h,i) Varying solid density. (a,d,g) Clamped area boundary condition on the 3-D solid ring. (b,e,h) Free area boundary condition on the 3-D solid ring. (c,f,i) Continuity of the area at the coupling interfaces.

where the continuity of the area is imposed, and the other two types of boundary conditions. More precisely, in the former case a refinement of the mesh leads to a progressive reduction of the reflection amplitude. On the contrary, in the latter approaches, the same refinement increases the reflection. Finally, note that a similar analysis with respect to the 1-D mesh size does not produce any significant difference. In particular, below a certain mesh size, the results in the 1-D segment are almost the same.

5.2. From 3-D to 1-D wave flow propagation. In the second case, described in Figure 5.4, we study the reflection amplitude generated at the coupling interfaces when a wave propagates from a 3-D FSI pipe (on the left) to a 1-D FSI segment (on the right), see Figure 5.4(a). We consider as a reference case the solution computed by solving the problem in Figure 5.4(b), i.e., a single 3-D pipe of length 6.

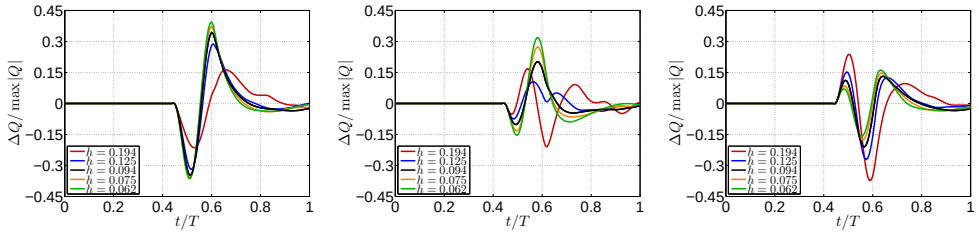

(a) (b) (c)

Figure 5.3: Volumetric flow rate wave reflection at the coupling interfaces for different values of the fluid mesh size (note that also the solid mesh size changes accordingly). As in Figure 5.2, the black curve corresponds to the reference parameters. (a) Clamped area boundary condition on the 3-D solid ring. (b) Free area boundary condition on the 3-D solid ring. (c) Continuity of the area at the coupling interfaces.

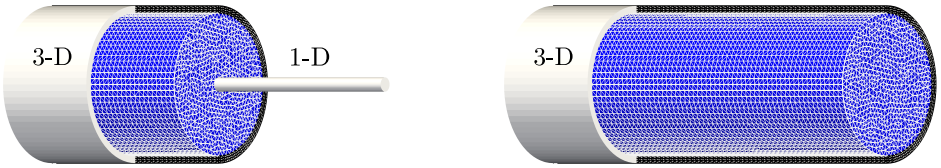

(a) (b)

Figure 5.4: Schematic representation of the benchmark case. (a) The wave flow propagates from the 3-D FSI model to the 1-D FSI one. The length of each pipe is equal to 3. (b) The reference case: a single 3-D FSI pipe of length 6.

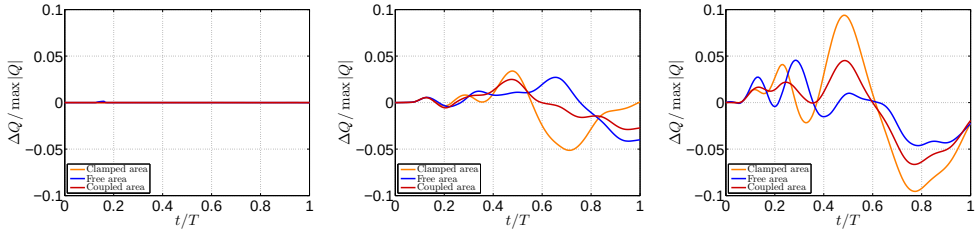

(a) (b) (c)

Figure 5.5: Volumetric flow rate wave reflection at different locations of the 3-D FSI pipe. (a) Left inlet. (b) Half section. (c) Right outlet (coupling interface).

In Figure 5.5 we plot the same quantities that we use in Figure 5.2 for the inverted configuration. By comparing the reflection amplitude in Figure 5.2 with the results in Figure 5.5(c), we observe that in the latter case the amplitude of the reflection is much smaller, around one-third of the former case. This behavior can be explained by observing that the 1-D problem is hyperbolic and at the coupling interface it

behaves as a passive element which absorbs the flow generated by the 3-D pipe. On the contrary, in the former case, the flow generated by the 1-D segment is passed to a non-hyperbolic model which returns an active feedback to the connected 1-D segment.

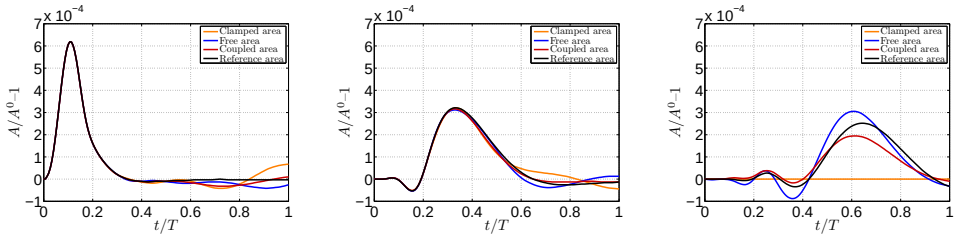

(a) (b) (c)

Figure 5.6: Percent variation of the area of the 3-D FSI pipe in Figure 5.4(a) at different locations. The black line is the reference area (see Figure 5.4(b)). (a) Left inlet. (b) Half section. (c) Right outlet (coupling interface).

Finally, a further comparison can be made between the results obtained with the different interface conditions for the solid problem. This analysis leads to the same conclusions discussed in Section 5.1. In particular, the amplitude of the reflection is always larger when the 3-D solid ring is clamped, while the other two approaches yield similar results. However, by inspecting the results in Figure 5.6, it follows that prescribing the continuity of the area of the pipes produces a slightly better result with respect to letting the deformation of the 3-D boundary solid ring free.

6. Computational cost analysis in abdominal aorta simulation. In order to assess the efficiency of the methodology presented here, we compare the number of iterations and the CPU time required to solve a realistic flow simulation as a function of several parameters, i.e., the 3-D FSI time discretization scheme, the number of coupling interfaces, and the algorithm to solve the interface problem. To perform this analysis we select a 3-D geometry of an arterial abdominal aorta, equipped with six coupling interfaces. At each boundary interface we connect a 1-D pipe featuring a length of 1.5 cm and a uniform reference area equal to the one of the nearby fluid interface of the 3-D FSI abdominal aorta. The interface problem is defined by imposing the coupling flow on all the six coupling interfaces, while all the boundary rings of the 3-D solid problem are clamped. The problem is finally closed by imposing six periodic volumetric flow rate profiles on the other sides of the 1-D pipes, as shown in Figure 6.1. These data have been taken from the solution of the full 1-D arterial tree described in [14, Section 5].

Regarding the wall parameters we use the same values provided in [14]. On the solid external wall $\Gamma^0_{S,ext}$ of the 3-D FSI abdominal aorta we apply a proper Robin boundary condition, which takes into account also the viscoelastic effects of the arterial wall, while we set $\phi_S = 10°$, $T_S = 0.24$ s, and $P_{ext} = 100000$ dyn/cm^2 for the 1-D FSI pipes. The Poisson ratio ν_S is 0.5 for the 1-D FSI pipes and 0.475 for the 3-D FSI abdominal aorta. The thickness of the vessel walls has been set equal to 10% of the local radius. Finally, the other parameters that define the problem are: $\rho_F = 1.04$ g/cm^3, $\mu_F = 0.035$ g/cm/s, $\alpha_F = 1.1$, $E_S = 3000000$ dyn/cm^2, and $\rho_S = 1.2$ g/cm^3.

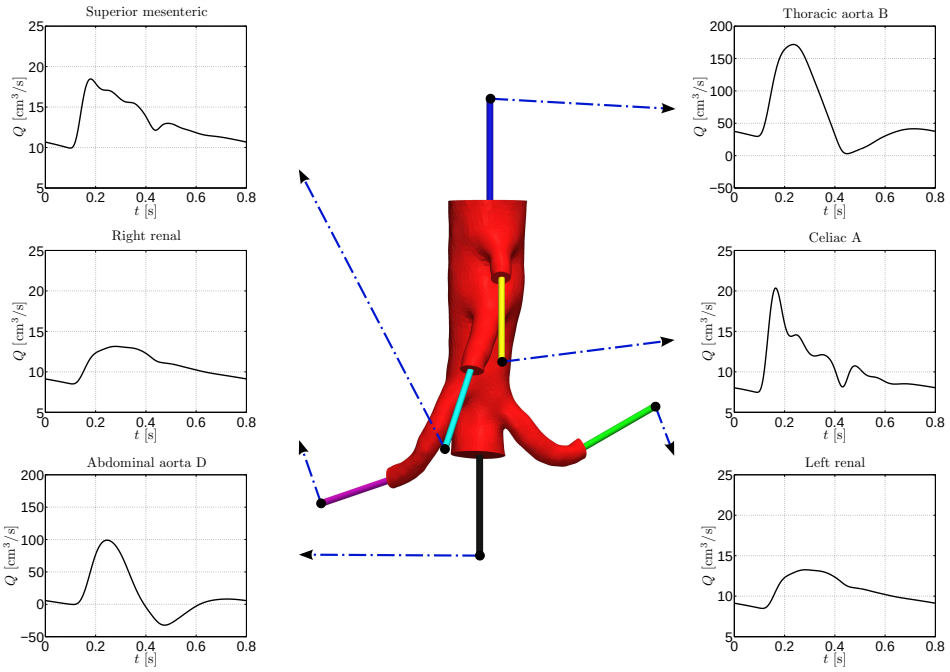

Figure 6.1: View of the 3-D FSI abdominal aorta (red color) coupled with six 1-D FSI arterial segments (other colors). On the two sides of the image, the periodic inflow/outflow volumetric flow rate profiles imposed on the six 1-D pipes are shown. More precisely, the flow imposed at the top of the 1-D thoracic aorta segment (top-right figure) is incoming, while the other five flows are outgoing.

The imposed tolerance for the interface problem is 10^{-6}, while the one for the 3-D FSI problem is 10^{-7}. The mesh of the fluid part of the 3-D abdominal aorta consists of 361969 tetrahedral elements with 62741 vertices, while the solid part is made of 236004 tetrahedral elements with 49675 vertices. The corresponding average space discretizations for the fluid and solid problems are 0.026 cm and 0.044 cm, respectively. Regarding the 1-D FSI segments, we use a uniform space discretization of 0.1 cm, corresponding to 16 vertices. The global time step is set equal to 10^{-3} s. All the simulations were performed on five cluster nodes with two Intel® Xeon® processors X5550 (quad core, 8 MB cache, 2.66 GHz CPU) each, for a total of 40 CPUs interconnected by a 20 Gb/s InfiniBand® architecture.

To set up the comparison we firstly run three heart beats of the problem described in Figure 6.1, to reach a quasi-periodic solution in the entire network. Then, starting from this initial condition, we run twenty time steps (corresponding to 0.020 s) for several configurations. Each of these configurations is set by removing one by one the 1-D segments from the initial problem. More precisely, from the initial configuration in Figure 6.1, the 1-D pipes are removed in the following order: left renal (green), right renal (magenta), superior mesenteric (ciano), celiac A (yellow), abdominal aorta D (black), and, finally, thoracic aorta B (blue). Note that, to preserve the same physics of the problem, each removed 1-D pipe has been replaced with the corresponding boundary volumetric flow rate profile of the fully coupled problem. Finally, we com-

pute the average number of iterations per time step required for the solution of the interface problem and the CPU time of the entire simulation normalized over the CPU time needed by the reference case, i.e., the 3-D FSI abdominal aorta discretized by a GCE scheme and without any coupled 1-D segment. The results of this comparison are summarized in Table 6.1 and 6.2.

Table 6.1: Average number of coupling iterations required for the simulation of the 3-D FSI abdominal aorta coupled with a progressively decreasing number of 1-D segments. The average number of Newton iterations for the convergence of the FI 3-D FSI problem is 3.88.

	GCE		FI	
1-D pipes	Newton	Broyden	Newton	Broyden
6	2.00	2.00	7.95	9.15
5	2.00	2.00	7.20	9.05
4	2.00	2.00	6.05	8.00
3	2.00	2.00	6.00	7.75
2	1.75	2.00	6.00	7.90
1	1.25	1.95	5.95	7.70

Table 6.2: Relative CPU time required for the simulation of the 3-D FSI abdominal aorta coupled with a progressively decreasing number of 1-D segments. In the last two columns, the values in the parentheses correspond to the same CPU times normalized over the CPU time needed by the FI reference case, which is 5.13 times slower than the GCE one.

	GCE		FI	
1-D pipes	Newton	Broyden	Newton	Broyden
6	9.91	2.33	120.20 [23.42]	45.46 [8.86]
5	8.58	2.30	94.09 [18.34]	44.93 [8.76]
4	7.20	2.26	67.77 [13.21]	40.22 [7.84]
3	6.00	2.23	57.08 [11.13]	39.04 [7.61]
2	4.29	2.20	47.99 [9.35]	39.64 [7.73]
1	2.27	2.15	36.33 [7.08]	38.65 [7.53]

From the analysis of these results, we draw that increasing the number of coupling nodes, which yields an increase of the size of the interface problem, does not produce a significant variation of the average number of iterations required to solve the coupled problem. A similar consideration holds comparing the results for the two solution algorithms. More precisely, the Newton method behaves as the Broyden one in the case of a GCE time discretization, and slightly better than Broyden method in the FI approach. On the contrary, there is a visible increase in the average number of iterations between the GCE and the FI time discretizations schemes. This is due to the strong nonlinearities of the FI approach.

Regarding the CPU time, we observe a quite different behavior. In particular,

the Newton method shows a strong dependence from the number of coupling nodes of the problem. This is justified by the fact that, in this example, each coupling node requires the computation of two additional Jacobian entries which, in turn, requires the additional solution of a 3-D FSI tangent problem and of a 1-D FSI model (to perform the finite difference approximation), at each nonlinear Richardson iteration. On the contrary, the CPU time required to solve the interface problem with the Broyden method is almost the same. More precisely, by using the Broyden method the CPU time required to solve the coupled problem is about 2.3 and 5 times the one required to solve the uncoupled 3-D FSI model discretized with the GCE and FI time discretization approaches, respectively. Last but not least, it is interesting to notice that there is an increase of more than one order of magnitude in the CPU time required for the solution of the coupled problem when using the FI approach with respect to the GCE case.

In view of these considerations, it is clear that from the computational viewpoint the Broyden method performs much better than the Newton method. In addition, the use of a GCE time discretization is recommended, unless additional motivations arises justifying the use of the more expensive FI approach. Further comparisons between these two approaches, with a focus on the main physical quantities, are addressed in [12].

7. Conclusions. In this work, we presented a numerical technique for the coupling of 1-D and 3-D FSI models for arterial networks. A full description of the FSI models equations has been provided, together with the strategies used to solve the numerical problems.

The global network of elements is solved by using a partitioned approach, where the models communicate only through the exchange of averaged/integrated quantities across the boundary interfaces. In particular, the fluid coupling equations are based on the conservation of the volumetric flow rate and on the continuity of the average of the normal component of the traction vector. Regarding the solid part of the problems, since the 1-D FSI model is already closed by the fluid coupling equations, we mainly focus on the 3-D FSI one. More precisely, we devise three different sets of boundary conditions to close the 3-D solid problem. All of them are stand-alone boundary conditions, that can be employed with and without connected 1-D models. Moreover the third one can be further extended to account for the continuity of the vessel area between the 3-D and 1-D FSI problems.

The problem at the coupling interfaces is solved by a classical nonlinear Richardson approach. In particular, two different numerical strategies have been selected: the Newton/inexact-Newton and the Broyden methods. The former requires the computation/approximation of the Jacobian matrix: for the 3-D FSI model this is done by solving the associated tangent problem, while for the 1-D FSI problem a finite difference approximation scheme is used. Regarding the Broyden method, it is based just on the evaluation of the residual, leading to a very cheap formulation. Note however that the Broyden matrix needs to be initialized with a good approximation of the Jacobian, which can be retrieved by using the former method.

The methodology presented here has been tested on several cases, ranging from simple benchmark examples, consisting in serial connection of pipes, to a more physiological example in the arterial network. The former case has been used to carry out a sensitivity analysis of the spurious backward reflections that might be generated at the coupling interfaces between the dimensionally-heterogeneous models. The latter, served to set up a comparison in terms of number of iterations and CPU time be-

tween the different solution algorithms; indeed it also proved the robustness of the methodology devised here under physiological conditions.

Acknowledgements. A. C. I. Malossi, P. Crosetto, S. Deparis, and A. Quarteroni acknowledge the European Research Council Advanced Grant "Mathcard, Mathematical Modelling and Simulation of the Cardiovascular System", Project ERC-2008-AdG 227058, and the Swiss Platform for High-Performance and High-Productivity Computing (HP2C). P. J. Blanco acknowledges the support of the Brazilian agencies CNPq and FAPERJ. We also acknowledge the support of the Brazilian–Swiss Joint Research Programme (BSJRP), Project BJRP 011010 (N 590002/2010-4). All the numerical results presented in this paper have been computed using the `LifeV` library (www.lifev.org).

REFERENCES

[1] S. J. Sherwin, V. Franke, J. Peiró, and K. Parker, *One-dimensional modelling of a vascular network in space-time variables*, J. Eng. Math., 47 (2003), pp. 217–250.

[2] L. Formaggia, D. Lamponi, and A. Quarteroni, *One-dimensional models for blood flow in arteries*, J. Eng. Math., 47 (2003), pp. 251–276.

[3] P. J. Blanco, J. S. Leiva, R. A. Feijóo, and G. C. Buscaglia, *Black-box decomposition approach for computational hemodynamics: One-dimensional models*, Comp. Meth. Appl. Mech. Engrg., 200 (2011), pp. 1389–1405.

[4] I. E. Vignon-Clementel, C. A. Figueroa, K. E. Jansen, and C. A. Taylor, *Outflow boundary conditions for three–dimensional finite element modeling of blood flow and pressure in arteries*, Comp. Meth. Appl. Mech. Engrg., 195 (2006), pp. 3776–3796.

[5] F. Nobile and C. Vergara, *An effective fluid-structure interaction formulation for vascular dynamics by generalized Robin conditions*, SIAM J. Sci. Comput., 30 (2008), pp. 731–763.

[6] H. J. Kim, I. E. Vignon-Clementel, C. A. Figueroa, J. F. LaDisa, K. E. Jansen, J. A. Feinstein, and C. A. Taylor, *On coupling a lumped parameter heart model and a three-dimensional finite element aorta model*, Ann. Biomed. Eng., 37 (2009), pp. 2153–2169.

[7] H. G. Matthies and J. Steindorf, *Partitioned strong coupling algorithms for fluid-structure interaction*, Comput. Struct., 81 (2003), pp. 805–812. K.J Bathe 60th Anniversary Issue.

[8] S. Deparis, M. Discacciati, G. Fourestey, and A. Quarteroni, *Fluid-structure algorithm based on Steklov–Poincaré operators*, Comp. Meth. Appl. Mech. Engrg., 195 (2006), pp. 5797–5812.

[9] T. E. Tezduyar, S. Sathe, and K. Stein, *Solution techniques for the fully discretized equations in computation of fluid-structure interactions with the space-time formulations*, Comp. Meth. Appl. Mech. Engrg., 195 (2006), pp. 5743–5753.

[10] Y. Bazilevs, V. M. Calo, T. J. R. Hughes, and Y. Zhang, *Isogeometric fluid-structure interaction: theory, algorithms, and computations*, Comput. Mech., 43 (2008), pp. 3–37.

[11] U. Küttler, M. Gee, C. Förster, A. Comerford, and W. A. Wall, *Coupling strategies for biomedical fluid-structure interaction problems*, Int. J. Num. Meth. Biomed. Engng., 26 (2010), pp. 305–321.

[12] P. Crosetto, *Fluid-Structure Interaction Problems in Hemodynamics: Parallel Solvers, Preconditioners, and Applications*, PhD thesis, EPFL, 2011.

[13] P. Reymond, F. Merenda, F. Perren, D. Rüfenacht, and N. Stergiopulos, *Validation of a one-dimensional model of the systemic arterial tree*, Am. J. Physiol. Heart Circ. Physiol., 297 (2009), pp. H208–H222.

[14] A. C. I. Malossi, P. J. Blanco, and S. Deparis, *A two-level time step technique for the partitioned solution of one-dimensional arterial networks*. Submitted, 2011.

[15] J. T. Ottesen, M. S. Olufsen, and J. K. Larsen, *Applied Mathematical Models in Human Physiology*, vol. MM09 of Monographs on Mathematical Modeling and Computation, SIAM, 2004.

[16] L. Formaggia, A. Quarteroni, and A. Veneziani, *Cardiovascular Mathematics*, vol. 1 of Modeling, Simulation and Applications, Springer, Milan, 2009.

[17] L. Formaggia, D. Lamponi, M. Tuveri, and A. Veneziani, *Numerical modeling of 1D arterial networks coupled with a lumped parameters description of the heart*, Comput. Methods Biomech. Biomed. Engin., 9 (2006), pp. 273–288.

[18] L. Grinberg and G. E. Karniadakis, *Outflow boundary conditions for arterial networks with multiple outlets*, Ann. Biomed. Eng., 36 (2008), pp. 1496–1514.
[19] P. J. Blanco, S. A. Urquiza, and R. A. Feijóo, *Assessing the influence of heart rate in local hemodynamics through coupled 3D-1D-0D models*, Int. J. Num. Meth. Biomed. Engng., 26 (2010), pp. 890–903.
[20] A. C. I. Malossi, P. J. Blanco, S. Deparis, and A. Quarteroni, *Algorithms for the partitioned solution of weakly coupled fluid models for cardiovascular flows*, Int. J. Num. Meth. Biomed. Engng., 27 (2011), pp. 2035–2057.
[21] L. Formaggia, A. Moura, and F. Nobile, *On the stability of the coupling of 3D and 1D fluid-structure interaction models for blood flow simulations*, ESAIM: Mathematical Modelling and Numerical Analysis, 41 (2007), pp. 743–769.
[22] L. Formaggia, J.-F. Gerbeau, F. Nobile, and A. Quarteroni, *On the coupling of 3D and 1D Navier–Stokes equations for flow problems in compliant vessels*, Comp. Meth. Appl. Mech. Engrg., 191 (2001), pp. 561–582.
[23] P. J. Blanco, R. A. Feijóo, and S. A. Urquiza, *A unified variational approach for coupling 3D–1D models and its blood flow applications*, Comp. Meth. Appl. Mech. Engrg., 196 (2007), pp. 4391–4410.
[24] P. Crosetto, S. Deparis, G. Fourestey, and A. Quarteroni, *Parallel algorithms for fluid-structure interaction problems in haemodynamics*, SIAM J. Sci. Comput., 33 (2011), pp. 1598–1622.
[25] L. Formaggia, A. Quarteroni, and C. Vergara, *On the physical consistency of the coupling between three-dimensional compliant and one-dimensional problems in haemodynamics*. Submitted, 2012.
[26] L. Formaggia and F. Nobile, *A stability analysis for the arbitrary Lagrangian Eulerian formulation with finite elements*, East-West J. Numer. Math., 7 (1999), pp. 105–131.
[27] P. Moireau, N. Xiao, M. Astorino, C. A. Figueroa, D. Chapelle, C.-A. Taylor, and J.-F. Gerbeau., *External tissue support and fluid-structure simulation in blood flows*, Biomech. Model. Mechanobiol., (2011).
[28] S. Deparis, M. Discacciati, and A. Quarteroni, *A domain decomposition framework for fluid-structure interaction problems*, in Proceedings of the Third International Conference on Computational Fluid Dynamics (ICCFD3), Springer Berlin Heidelberg, 2006, pp. 41–58.
[29] P. Causin, J.-F. Gerbeau, and F. Nobile, *Added-mass effect in the design of partitioned algorithms for fluid-structure problems*, Comp. Meth. Appl. Mech. Engrg., 194 (2005), pp. 4506–4527.
[30] S. Badia, F. Nobile, and C. Vergara, *Fluid-structure partitioned procedures based on robin transmission conditions*, J. Comput. Phys., 227 (2008), pp. 7027–7051.
[31] L. Gerardo-Giorda, F. Nobile, and C. Vergara, *Analysis and optimization of Robin–Robin partitioned procedures in fluid-structure interaction problems*, SIAM J. Sci. Comput., 48 (2010), pp. 2091–2116.
[32] E. Burman, M. A. Fernández, and P. Hansbo, *Continuous interior penalty finite element method for Oseen's equations*, SIAM J. Numer. Anal., 44 (2006), pp. 1248–1274.
[33] M. A. Fernández and M. Moubachir, *A Newton method using exact Jacobian for solving fluid-structure coupling*, Comput. Struct., 83 (2005), pp. 127–142.
[34] A. Quarteroni and A. Veneziani, *Analysis of a geometrical multiscale model based on the coupling of ODEs and PDEs for blood flow simulations*, SIAM J. Multiscale Model. Simul., 1 (2003), pp. 173–195.
[35] A. Quarteroni and L. Formaggia, *Modelling of Living Systems*, Handbook of Numerical Analysis Series, Elsevier, 2003, ch. Mathematical Modelling and Numerical Simulation of the Cardiovascular System.
[36] T. Passerini, M. de Luca, L. Formaggia, A. Quarteroni, and A. Veneziani, *A 3D/1D geometrical multiscale model of cerebral vasculature*, J. Eng. Math., 64 (2009), pp. 319–330.
[37] L. Quartapelle, *Numerical Solution of the Incompressible Navier–Stokes Equations*, vol. 113 of International Series of Numerical Mathematics, Birkhäuser Verlag, Basel, 1993.
[38] L. Formaggia, J.-F. Gerbeau, F. Nobile, and A. Quarteroni, *Numerical treatment of defective boundary conditions for the Navier–Stokes equations*, SIAM J. Numer. Anal., 40 (2002), pp. 376–401.
[39] J. G. Heywood, R. Rannacher, and S. Turek, *Artificial boundaries and flux and pressure conditions for the incompressible Navier–Stokes equations*, Int. J. Num. Meth. Fluids, 22 (1996), pp. 325–352.
[40] J. S. Leiva, P. J. Blanco, and G. C. Buscaglia, *Partitioned analysis for dimensionally-heterogeneous hydraulic networks*, SIAM J. Multiscale Model. Simul., 9 (2011), pp. 872–903.

Recent publications :

MATHEMATICS INSTITUTE OF COMPUTATIONAL SCIENCE AND ENGINEERING
Section of Mathematics
Ecole Polytechnique Fédérale
CH-1015 Lausanne

01.2012 A. ABDULLE, A. NONNENMACHER:
A posteriori error estimate in quantities of interest for the finite element heterogeneous multiscale method

02.2012 F. NOBILE, M. POZZOLI, C. VERGARA:
Time accurate partitioned algorithms for the solution of fluid-structure interaction problems in haemodynamics

03.2012 T. LASSILA, A. MANZONI, A. QUARTERONI, G. ROZZA:
Boundary control and shape optimization for the robust design of bypass anastomoses under uncertainty

04.2012 D. KRESSNER, C. TOBLER:
htucker – A Matlab toolbox for tensors in hierarchical Tucker format

05.2012 A. ABDULLE, G. VILLMART, KONSTANTINOS C. ZYGALAKIS:
Second weak order explicit stabilized methods for stiff stochastic differential equations.

06.2012 A. CABOUSSAT, S. BOYAVAL, A. MASSEREY:
Three-dimensional simulation of dam break flows.

07.2012 J BONNEMAIN, S. DEPARIS, A. QUARTERONI:
Connecting ventricular assist devices to the aorta: a numerical model.

08.2012 J BONNEMAIN, ELENA FAGGIANO, A. QUARTERONI, S. DEPARIS:
A framework for the analysis of the haemodynamics in patient with ventricular assist device.

09.2012 TONI LASSILA, ANDREA MANZONI GIANLUIGI ROZZA:
Reduction strategies for shape dependent inverse problems in haemodynamics.

10.2012 C. MALOSSI, P. BLANCO, P. CROSETTO, S. DEPARIS, A. QUARTERONI:
Implicit coupling of one-dimensional and three-dimensional blood flow models with compliant vessels.